



**HAL**  
open science

## Methylene blue removal from aqueous solutions using a biochar/gellan gum hydrogel composite: Effect of agitation mode on sorption kinetics

Ahmed Elgarahy, Hamida Mostafa, Elsayed Zaki, Shymaa Elsaheed, Khalid Elwakeel, Abdullah Akhdhar, Guibal Eric

### ► To cite this version:

Ahmed Elgarahy, Hamida Mostafa, Elsayed Zaki, Shymaa Elsaheed, Khalid Elwakeel, et al.. Methylene blue removal from aqueous solutions using a biochar/gellan gum hydrogel composite: Effect of agitation mode on sorption kinetics. *International Journal of Biological Macromolecules*, 2023, 232, pp.123355. 10.1016/j.ijbiomac.2023.123355 . hal-03975151

**HAL Id: hal-03975151**

**<https://hal.science/hal-03975151>**

Submitted on 20 Mar 2023

**HAL** is a multi-disciplinary open access archive for the deposit and dissemination of scientific research documents, whether they are published or not. The documents may come from teaching and research institutions in France or abroad, or from public or private research centers.

L'archive ouverte pluridisciplinaire **HAL**, est destinée au dépôt et à la diffusion de documents scientifiques de niveau recherche, publiés ou non, émanant des établissements d'enseignement et de recherche français ou étrangers, des laboratoires publics ou privés.

# Methylene blue removal from aqueous solutions using a biochar/gellan gum hydrogel composite: Effect of agitation mode on sorption kinetics

Ahmed M. Elgarahy<sup>a,b</sup>, Hamida Y. Mostafa<sup>c</sup>, Elsayed G. Zaki<sup>c</sup>, Shymaa M. ElSaeed<sup>c</sup>, Khalid Z. Elwakeel<sup>a,d,\*</sup>, Abdullah Akhdhar<sup>d</sup>, Eric Guibal<sup>e,\*\*</sup>

<sup>a</sup> Environmental Chemistry Division, Environmental Science Department, Faculty of Science, Port Said University, Port Said, Egypt

<sup>b</sup> Egyptian Propylene and Polypropylene Company (EPPC), Port Said, Egypt

<sup>c</sup> Egyptian Petroleum Research Institute, Nasr City 11727, Cairo, Egypt

<sup>d</sup> University of Jeddah, College of Science, Department of Chemistry, Jeddah, Saudi Arabia

<sup>e</sup> Polymers Composites and Hybrids (PCH), IMT Mines Ales, Alès, France

## A B S T R A C T

Hydrogel membranes are prepared by casting a mixture of gellan gum (associated with PVA) and biochar produced from a local Egyptian plant. The mesoporous material is characterized by a specific surface area close to  $134 \text{ m}^2 \text{ g}^{-1}$ , a residue of 28 % (at  $800^\circ\text{C}$ ), and a  $\text{pH}_{\text{PZC}}$  close to 6.43. After grinding, the material is tested for Methylene Blue sorption at pH 10.5: sorption capacity reaches  $1.70 \text{ mmol MB g}^{-1}$  (synergistic effect of the precursors). The sorption isotherms are fitted by both Langmuir and Sips eqs. MB sorption increases with temperature: the sorption is endothermic ( $\Delta H^\circ: 12.9 \text{ kJ mol}^{-1}$ ), with positive entropy ( $\Delta S^\circ: 125 \text{ J mol}^{-1} \text{ K}^{-1}$ ). Uptake kinetics are controlled by agitation speed (optimum  $\approx 200 \text{ rpm}$ ) and resistance to intraparticle diffusion. The profiles are strongly affected by the mode of agitation: the equilibrium time ( $\approx 180 \text{ min}$ ) is reduced to 20–30 min under sonication (especially at frequency: 80 kHz). The mode of agitation controls the best fitting equation: pseudo-first order rate agitation for mechanical agitation contrary to pseudo-second order rate under sonication. The sorption of MB is poorly affected by ionic strength (loss  $< 6 \%$  in  $45 \text{ g L}^{-1}$  NaCl solution). Desorption (faster than sorption) is completely achieved using 0.7 M HCl solution. At the sixth recycling, the loss in sorption is close to 5 % ( $\approx$  decrease in desorption efficiency). The process is successfully applied for the treatment of MB-spiked industrial solution: the color index decreases by  $> 97 \%$  with a sorbent dose close to  $1 \text{ g L}^{-1}$ ; a higher dose is required for maximum reduction of the COD (60 % at  $3 \text{ g L}^{-1}$ ).

### Keywords:

Mesoporous gellan gum (GG)/PVA-biochar composite  
Methylene blue sorption from alkaline solutions  
Sonication effects on kinetics  
Sorption/desorption kinetics

## 1. Introduction

The scarcity of natural water resources (especially under the effect of climate change and global warming), and the increasing demand for water in domestic, agricultural, and industrial uses explain the incentive politics for reclaiming wastewater for decontamination and re-use. One of the evident consequences consists of the reinforcement of national and regional regulations concerning the discharge of wastewater into the environment. Though the attention strongly focuses on the behavior of inorganic and metal ions in the environment, great attention is paid to organic pollutants such as drugs, pharmaceutical molecules but also dyes. Independently of their intrinsic toxicity, dyes may also affect water bodies through perturbations to photosynthetic activity (coloring

effect). These dual impacts may explain the intense research activity on the treatment of colored effluents. The processes for dye removal may involve precipitation and flotation [1–3], and solvent extraction [4–6]. Catalytic and photocatalytic degradation have been also widely documented [7–10]. It is noteworthy that the degradation of organic compounds by the catalytic process may, in certain cases, produce even more hazardous compounds than the precursors [11,12]. Sorption represents an alternative strategy for the recovery of dyes from aqueous solutions, using low-cost bio-based sorbents [13,14], chitosan, and derivatives [15–17]. Nano-based materials [18], resins [19–21], and silica [22–24] have also been referenced for their efficiency in dye removal. Activated carbon (AC) is an interesting resource for designing dye sorbents, taking advantage of its high specific surface area [25,26]. Biochar offers a cost-

\* Co-corresponding author.

\*\* Corresponding author at: Polymers Composites and Hybrids (PCH), IMT Mines Ales, Alès, France.

E-mail addresses: [khalid\\_elwakeel@yahoo.com](mailto:khalid_elwakeel@yahoo.com) (K.Z. Elwakeel), [eric.guibal@mines-ales.fr](mailto:eric.guibal@mines-ales.fr) (E. Guibal).

effective alternative to AC (obtained by pyrolysis of biomass) for the remediation of dyes from aqueous solutions [27–30]. Tan et al. [31] reviewed the numerous possibilities of the application of biochar for wastewater decontamination and reported some of the challenges to be ruled out for ensuring the development of biochar-based sorbents; including the practical operating conditions for sorption and desorption processing. Composite materials based on the reaction of biochar with other supports, or embedment in a polymer network represent some responses to these problems [32]. Currently, biochar and its derivatives have received special attention being intensively used in many applications in agronomy, construction, energy storage, environment, etc. [33]. These successful uses derive from their multifunctional properties (in terms of mechanical, thermal, catalytic characteristics, etc.). From the point of view of environmental applications, biochar has been used either alone or in combination with other materials to remove a wide range of contaminants, both organic and inorganic chemical species, from wastewater [34–37].

Gellan gum (GG) is a naturally occurring polysaccharide produced by *Sphingomonas elodea* as a linear extracellular polysaccharide. It is a linear heteropolysaccharide composed of D-glucose, D-glucuronic acid, and L-rhamnose repeating units with two acyl substituents, L-glyceryl, and acetyl, attached to the C-2 and C-6 positions of the O-3-linked 1,3-D-glucose residue [38]. Low acyl GG is produced via deacylation in an alkaline solution. Gellan polymer chains cannot create a tight double helix structure between chains because of bulky substituents. Since gellan gels are weak, soft, and elastic in their native form, reinforcements with additional materials (or complementary reactions) are usually required to achieve the desired mechanical properties [39]. It has already been tested for mass production (i.e., one company can produce over 500 tons of GG per year) [40]. Unlike other polysaccharides, GG maintains its gel state over a large range of pH in aqueous systems [41]. This feature offers exceptional acid-base stability, which makes it a good candidate to produce sorbents for the removal of organic contaminants at different pH values. In addition to being acid-base stable, GG exhibits very good thermal stability [42], performs very well in solutions with high ionic strength [43], and reacts well with organic dyes [44]. Despite these special properties, there has been little interest in using GG to remove contaminants from water until now. Examining the sorption capacity of GG or GG-based composites for contaminants and identifying the sorption mechanisms involved could pave the way for these materials to be used in green water and wastewater treatment technologies [45]. Therefore, GG hydrogel can have applications in the field of adsorption, due to its good biodegradability (at the end of its life cycle) and durability [46]. Gellan gum is a member of the broad exopolysaccharide family. In addition to hydrating in cold water with sequestrants, GG also hydrates in hot water in its low acyl form. When cooled, native high-acyl GG gives gels that are soft and elastic [45]. Combinations of GG with other materials can be used to control syneresis and form a range of textures from soft and elastic to firm and brittle.

In this context, the incorporation of biochar into the GG matrices may enhance the properties of the resulting composites because of the ability of biochar to affect the properties of the GG matrix. Gellan gum with biochar can gather the special advantages of biochar and GG including high surface area, high thermal and mechanical stability, and the flexibility of natural polymers. The use of natural materials (environmentally friendly) for the synthesis of sorbent composites has gained considerable interest from researchers in recent years. They are renewable, eco-friendly, biodegradable, and easily available.

In addition, the incorporation of polyvinyl alcohol (PVA) in the process promotes the formation of an interpenetrating network that contributes to improving mechanical properties and reducing uncontrolled swelling of polymer blends [47]. The film-forming properties are also well-known and useful for preparing membrane systems [48]. Therefore, the combination of dual polymers with the incorporation of biochar particles leads to new multifunctional materials with high

stability and promising sorption properties. These synergistic properties will be evaluated and compared to their precursors under different experimental conditions for Methylene Blue removal (as a model) for evaluating their potential in wastewater treatment.

Herein, the preferences for preparing a biochar composite are given to (a) the pyrolysis of *Orobancha aegyptiaca* biomass (endemic and Egyptian plant), and (b) the incorporation of the porous material into a biopolymer matrix (GG). Invasive *O. aegyptiaca* is of critical importance for local agriculture; therefore, the elimination and/or valorization of this harmful biomass is a strategic issue. Gelling of GG is processed by reaction with poly(vinyl alcohol) (PVA), which contributes to forming a polymeric network. Gellan gum has frequently been associated with synthetic polymers such as polyacrylic acid-based compounds [49–52], and amino-methacrylate derivatives [53], with eventually the incorporation of inorganic loads (montmorillonite, for example, [49]) for manufacturing composite hydrogels. The membrane is produced by casting. Its flexibility is enhanced by the incorporation of glycerol in the mixture (prior to casting).

First, the casted composite membrane (i.e., GG-BC) is characterized by scanning electron microscopy (SEM), transmission electron microscopy (TEM), N<sub>2</sub> adsorption/desorption (textural properties), thermogravimetric analysis (TGA, and differential scanning calorimetry, DSC), Fourier-transform infrared spectroscopy (FTIR) and zetametry.

The sorption properties are investigated for the recovery of methylene blue (MB, C<sub>16</sub>H<sub>18</sub>ClN<sub>3</sub>S), thiazine dye, Scheme S1, see Supplementary Information) using grinded composite membranes. The influence of environmental parameters is investigated (i.e., pH, sorbent dose, agitation speed, and addition of NaCl). Uptake kinetics and sorption isotherms are also collected and modeled using conventional equations. Special attention is paid to the effect of sonication (which is compared with mechanical agitation at different speeds) on the uptake kinetics. Dye desorption and sorbent recycling are carried out before investigating the recovery of the dye from a complex medium (i.e., spiked seawater samples).

## 2. Materials and methods

### 2.1. Materials

Gellan gum (GG, low acyl) with a molecular weight of  $2.4 \times 10^5$  Da) determined by gel permeation chromatography (was purchased from Alfa Aesar. Polyvinyl alcohol (PVA) (Mwt ~ 17–18 kDa) was purchased from the International Company for Chemicals (ICC, Al Khobar, Saudi Arabia). Glycerol (purity 99.5 %, Mwt ~ 92) was obtained from Al-Gomhoria Company (Zietoun, Cairo, Egypt), *Orobancha aegyptiaca* biomass was obtained locally from Damhoug, Quisna, Menofiya (Egypt).

### 2.2. Biochar production

Section A in Supplementary Information reports in detail the methods used for the production (and optimization) of the biochar through microwave-assisted extraction (MAE) and the proper carbonization procedure. Briefly, MAE process (Lab-made microwave equipment, with generator: 900 W and 2450 MHz frequency) was used for the extraction of polyphenolic compounds from *O. aegyptiaca* biomass (in aqueous suspension). Both the extraction time (0–20 min) and the power of the microwave oven (90, 180, and 270 W) were investigated and optimized [104]. The residue was recovered by filtration and used for preparing the biochar. Pyrolysis was carried out under N<sub>2</sub> atmosphere at 350 °C, for 3 h.

### 2.3. Sorbent synthesis

Gellan hydrogel membranes were prepared by the solution casting method [54]. Gellan (1 %, w/w) was dissolved in demineralized water at 80 °C under gentle stirring for 2 h (for avoiding the formation of air

bubbles). Polyvinylalcohol (PVA, 4 %, w/w) was dissolved in bi-distilled water at 70 °C under stirring for 2 h. Then PVA solution was added to the gellan solution and mixed with continuous stirring until complete miscibility. The ratio of gellan and PVA in the mixture was 80/20 (% , w/w).

The biochar (pyrolyzed *O. aegyptica* biochar) was ground, washed with 0.1 M HCl for 5 h, washed with demineralized water to remove any impurities, and then dried in an oven at 70 °C for 24 h. Pre-treated biochar (BC, 1 %, w/w) was added into the Gellan/PVA mixture and sonicated for 20 min to form a homogeneous dispersed solution. Glycerol (5 %, w/w, based on the final dry weight of polymer) was added under agitation. Finally, 20 mL of the mixture was poured into a glass petri dish (15 cm) and left to dry overnight at 60 °C in a vacuum oven. The films were peeled off from the glass disc, and stored, until use, in polyethylene bags to avoid contamination. Scheme 1 reports the different steps in the synthesis of the sorbent.

#### 2.4. Sorbent characterization

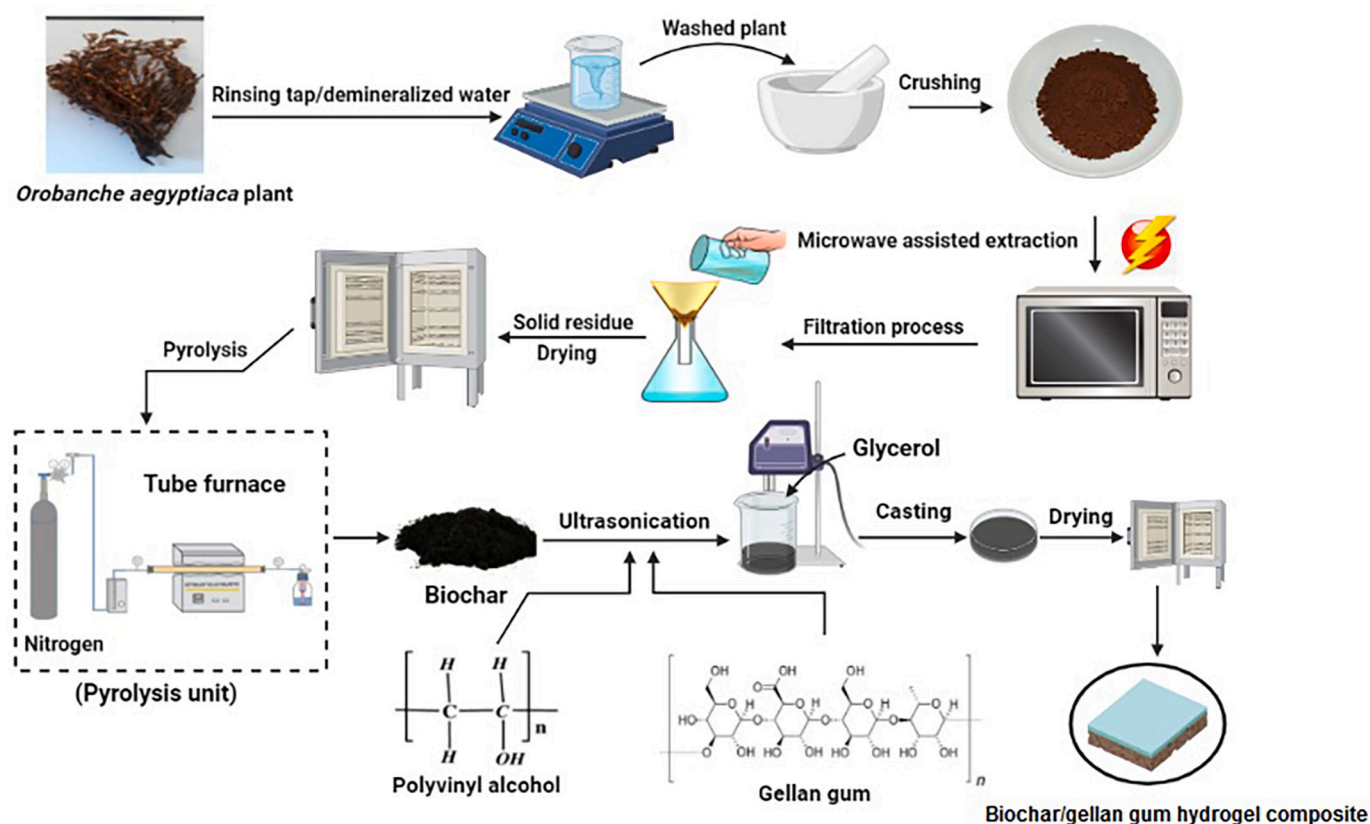
Waters Mass Spectrometers 515/2410 (Waters, USA) was used for measuring of molecular weight of the native GG using the gel permeation chromatography technique. The morphology and microstructure of the sorbent membrane (small pieces of the membrane with particle size in the range of 20–30 μm), were observed using a high-resolution transmission electron microscope (TEM, JEOL JEM 2100F, Tokyo, Japan). The images were taken at an accelerating voltage of 200kV. To prepare the TEM samples (cut and grinded), a particle-ethanol colloidal mixture was ultrasonicated for 20 min, and a drop of the suspension was placed on a grid and dried then the sample was examined. Surface morphology images have been obtained with a MEB-FEG scanning electron microscope Zeiss Sigma 300 VP – GEMINI, (Carl Zeiss Microscopy, Jena, Germany), equipped with a dispersive X-ray spectrometer (EDS). The thickness of membranes was measured with a 0–25 mm

electronic outside micrometer gauge meter 0.001 mm digital tool.

The sizes of the particles (biochar and composite sorbents) were analyzed by differential light scattering using Malvern Zetasizer Ver. 6.32 (Malvern Instruments Ltd., Malvern, UK). The thermal stability properties were characterized using a Q600 SDT thermal analyzer (Waters, TA instruments, New Castle, DE, USA), under N<sub>2</sub> atmosphere, with a heating rate of 10 °C min<sup>-1</sup> (from room temperature up to 1000 °C). The hydrophobic characteristics of membranes were determined by measurement of the contact angle (drop angle) using a T200 THETA optical tensiometer (Biolin Scientific AB, Västra Frölunda, Sweden). The X-ray diffraction analysis of the membrane was carried acquired using an X'Pert PRO X-ray diffractometer (Malvern Panalytical Ltd., Malvern, UK). The patterns were conducted using CuK<sub>α</sub> radiation (λ = 0.15406 nm). The 2θ angle varied between 4° and 70°. A Nano Zeta Sizer (Nano-ZS, Malvern Instruments, Malvern, UK) was used for the determination of the zeta potential of the composite sorbent and the native biochar and GG (sorbent dose, SD: 1 g L<sup>-1</sup>; 0.01 M KCl solution, pH<sub>0</sub>: 1–11; contact time before analysis: 4 h). FT-IR spectra were acquired using a Nicolet iS10 FTIR spectrometer (Thermo Scientific Instruments, Waltham, MA, USA).

#### 2.5. Sorption tests

The experiments were performed in batch systems (and duplicated). A fixed volume of solution (V, L), at C<sub>0</sub> concentration (mmol MB L<sup>-1</sup>), was mixed, at a standard speed of 200 rpm, (unless specified) with a given amount of sorbent (m, g) during fixed contact time. The standard temperature was 25 ± 1 °C (unless specified). The sorbent was separated from the solution by filtration (1.2-μm pore size membrane) and the residual concentration (C<sub>eq</sub>, mmol MB L<sup>-1</sup>) was analyzed by UV-Vis spectroscopy (Palintest 7100 spectrophotometer, Palintest Ltd., Gasteshead, UK) at λ: 664 nm wavelength (after adding a micro-drop of NaOH to shift the pH close to 10 for all samples calibration points and samples).



Scheme 1. Synthesis of precursors and sorbent.

The mass balance equation was used for determining the sorption capacity at equilibrium ( $q_{eq} = (C_0 - C_{eq}) \times V/m$ , mmol MB  $g^{-1}$ ). The solutions were not buffered, and the pH was not controlled during dye sorption; however, the final pH was systematically monitored using an Aqualytic AL15 pH meter (Aqualytic GmbH & Co, Dortmund, Germany).

Uptake kinetics were also obtained from batch tests; a four mL-volume sample was collected at fixed times for measuring actual dye concentration. The correction of volume was applied to deduce the sorption capacity (according to Eq. (1)).

$$q(t) = \sum_{i=1}^n \left( \frac{(C(t)_{(i-1)} - C(t)_{(i)}) \times V(t)_{(i-1)}}{m} \right) \quad (1)$$

For uptake kinetics performed under ultrasonic treatment, the sorption proceeded into a thermostatic box using an ultrasonic bath sonicator (Elmasonic P300H, Elma Schmidbauer GmbH, Singen, Germany). The power was 380 W while two frequencies were selected at 37 and 80 kHz.

For sorption isotherms, the initial concentration was varied from 0.0313 to 3.13 mmol MB  $L^{-1}$ , and the temperature was set at 25, 35, 45, and 55 °C. A shaking incubator was used for maintaining the appropriate temperature (LSI-3016R, LabTech S.r.l., Sorisole, BG, Italy). For studying the effect of NaCl concentration, the addition of the salt led to concentrations ranging between 0.086 and 0.77 mol NaCl  $L^{-1}$ . The impact of agitation speed on the sorption capacity at equilibrium was compared for velocities in the range of 50–300 rpm. The sorbent dose, SD, was varied between 0.5 and 5  $g L^{-1}$ . The experimental conditions are systematically reported in the caption of the figures (see below).

For dye desorption (in batch), an acidic solution (0.7 M HCl) was used. Sorption recycling was tested for six successive cycles (the water-rinsing step was systematically processed between each sorption and desorption operation).

## 2.6. Modeling of sorption kinetics and isotherms

Table S2a summarizes the equations used for modeling uptake kinetics: pseudo-first (PFORE), pseudo-second order rate (PSORE) equations [55], the Elovich equation [56], and the resistance to intraparticle diffusion (RIDE, the so-called Crank equation [57]). Resistance to intraparticle diffusion (RIDE) can be used for approaching the resistance to intraparticle diffusion. This equation was used for modeling the kinetic profile and approaching the determination of the effective intraparticle diffusion coefficient ( $D_e$ ,  $m^2 \text{ min}^{-1}$ ). Table S2b reports the equations used for fitting sorption isotherms: Langmuir, Freundlich, and Sips [58], Temkin [59], and Dubinin-Radushkevich (D-R) [60]. The quality of fitting was measured by the determination coefficient (i.e.,  $R^2$ ) and the Akaike Information Criterion (AIC, see Table S2b [61]).

For the determination of thermodynamic parameters, the van't Hoff equation was applied using the methodology reported by Tran et al. [62]. They documented the importance of the adjustment of parameter units for the appropriate determination of the equilibrium constant ( $K^{\circ}_{eq}$ ).

$$\Delta G^{\circ} = -RT \ln K^{\circ}_{eq} \quad (2)$$

$$\Delta G^{\circ} = \Delta H^{\circ} - T\Delta S^{\circ} \quad (3)$$

$\Delta G^{\circ}$  ( $\text{kJ mol}^{-1}$ ),  $R$  is the universal gas constant ( $8.31 \text{ J mol}^{-1} \text{ K}^{-1}$ ),  $\Delta H^{\circ}$  ( $\text{kJ mol}^{-1}$ ), and  $\Delta S^{\circ}$  ( $\text{J mol}^{-1} \text{ K}^{-1}$ ) are the changes in Gibbs energy, enthalpy, and entropy, respectively;  $R$  is the universal gas constant.

The equilibrium constant must be dimensionless for being consistent with thermodynamic criteria. Tran et al. [62] convert  $b_L$  affinity coefficient (in Langmuir equation) to equilibrium constant using the following equation:

$$K^{\circ}_{eq} = b_L \times \frac{C^{\circ}_{\text{Adsorbate}}}{\gamma_{\text{Adsorbate}}} \quad (4)$$

where  $C^{\circ}_{\text{Adsorbate}}$  is the unitary standard concentration of the adsorbate ( $\sim 1 \text{ mol L}^{-1}$ ) and  $\gamma_{\text{Adsorbate}}$  is the activity coefficient of the adsorbate (dimensionless); meaning that  $b_L$  should be converted to  $L \text{ mol}^{-1}$  unit.

## 3. Results and discussion

### 3.1. Characterization of sorbent

#### 3.1.1. Physical characterization of sorbent particles

The thickness ( $\tau$ , mm) of the composite membranes was measured using a digital micrometer gauge meter on several samples:  $\tau = 0.433 \pm 0.046$  mm, the membrane size fraction collected for sorption tests was 20–30 mm. all the adsorption studies were done using these small pieces of the membrane.

Fig. 1 shows the SEM micrographs of the sorbent (before and after MB sorption) at different magnitudes. The surface of the materials is irregular with aggregates and lamellar structures. The pristine material is characterized by opened channels (representative of the structure of raw material, *O. aegyptica* [63]) that disappear (being blocked) after dye binding.

Transmission electron microscopy (Fig. 2) shows relatively homogeneous structures with a light background associated with the GG matrix. The incorporation of biochar nano-objects is highlighted by little more obscure zones. The two components of the composite are constituted by light elements, which do not offer the possibility to isolate contrasting objects (as may appear when metal nanoparticles are embedded in composites). The sorption of MB hardly changes the TEM images of the sorbent. However, in Fig. 2, the left panel for MB-loaded sorbent shows more structured objects.

Differential light scattering (DLS) may be used for determining the size of biochar and sorbent particles (Fig. S1). The size of about 77.3 % of biochar nanoparticles are close to 196 nm (average value), however, a significant part (about 22.7%) has an average value close to 0.962  $\mu\text{m}$ . This is consistent with the order of magnitude of the largest objects observed in the composites (TEM image). The average size of the composite is found close to 1 mm.

#### 3.1.2. Thermal degradation of sorbent

Fig. S2 shows the thermal degradation of the composite sorbent (with TGA curve (a) and DTA/DSC profiles (b)). The degradation occurs through three steps:

(a) below 106 °C, free or absorbed water is released (representing a weight loss,  $WL \approx 6.3 \%$ ), (b) in the range 106–225 °C, most of the weight loss is registered ( $WL \approx 52.3 \%$ ); this phase corresponds to the release of –OH groups and the depolymerization of the GG network, and (c) above 225 °C, the formation of a char, followed by its thermal degradation  $WL \approx 29.2 \%$ .

These transitions are shifted to lower temperatures compared with the thermal degradation of free GG [64] and GG/PVA blends [65]. The total degradation reaches 72 %; this is consistent with the value reported for free GG by Tyagi et al. [66].

The DTA profile shows two local minima at  $T: 70.0 \text{ }^{\circ}\text{C}$  and  $206.1 \text{ }^{\circ}\text{C}$ , corresponding to the largest weight variations reported in TGA profiles. The DSC curve shows a weak relative minimum at  $208.9 \text{ }^{\circ}\text{C}$ ; this value is close to the temperature reported for minimum in DSC curve for GG-polyacrylamide composite (i.e.,  $237 \text{ }^{\circ}\text{C}$ , which is higher than the peak reported for GG alone) [64]. The PVA/glycerol interaction affects the thermal degradation characteristics of the composite. In the case of GG-PVA, it is noteworthy that the biochar that was pyrolyzed during the conversion of *O. aegyptica* may marginally contribute to the weight loss of the composite (consistent with conclusions raised on another type of biochar by Subratti et al. [67]).

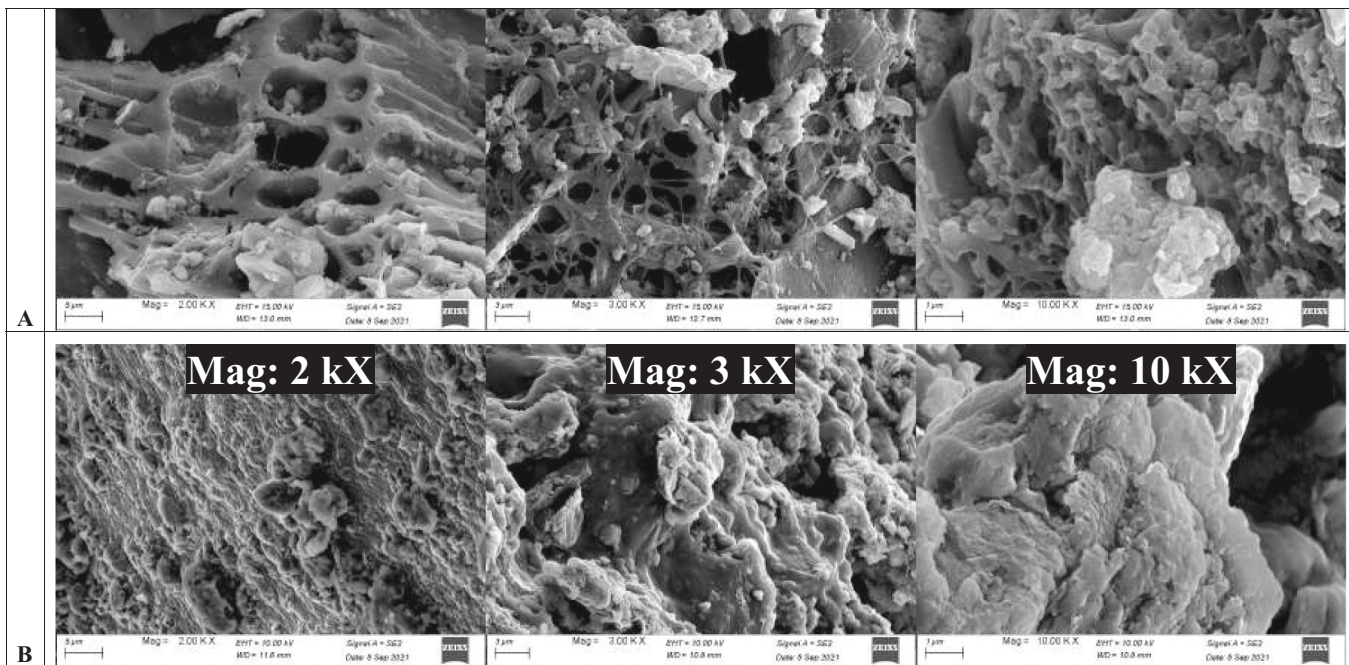


Fig. 1. SEM images of the sorbent before (A) and after (B) MB sorption (different growing magnitudes).

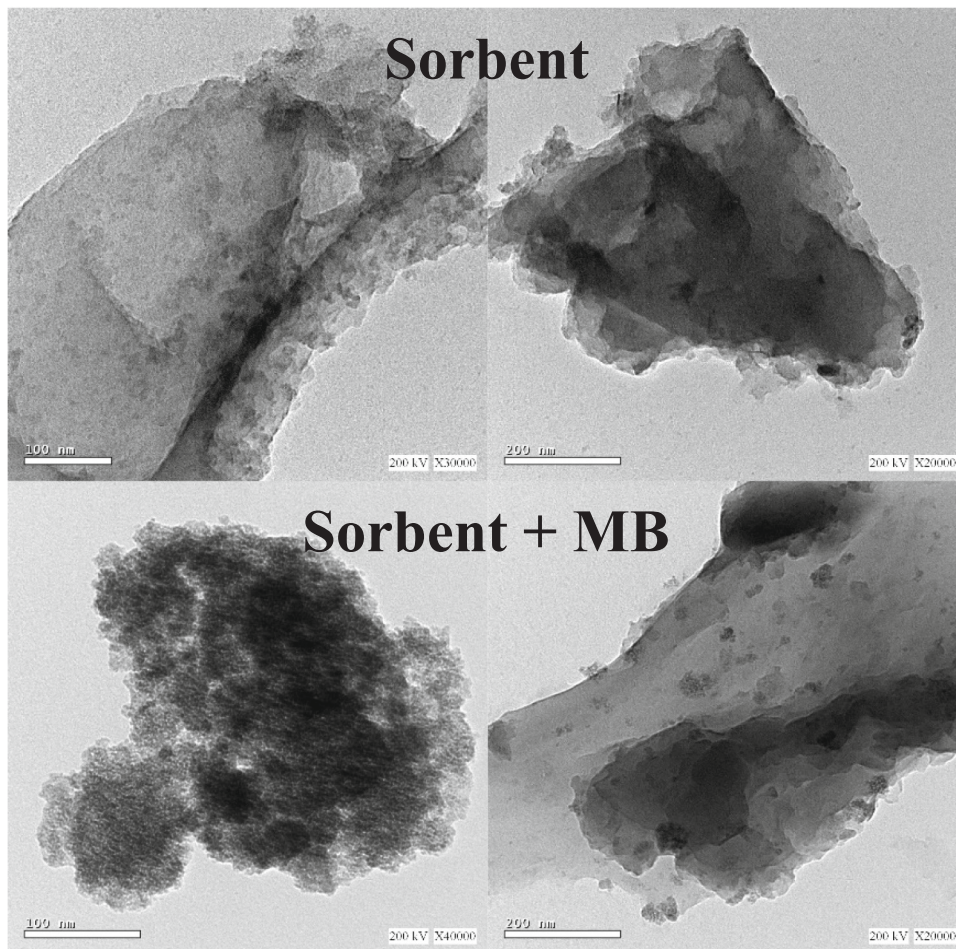


Fig. 2. TEM images of the sorbent before and after MB sorption (bar: left panels, 100 nm; right panels, 200 nm).

### 3.1.3. FTIR spectrometry

Fig. 3 compares the FTIR spectra of the composite sorbent as produced, after conditioning the sorbent at the pH used for MB sorption, and after dye binding. Table 1 summarizes the assignments of the main bands. The comparison of these spectra allows to separate the potential contributions of pH change (conditioned sorbent at fixed pH) from the interactions with the dye. The pH control (to 10.5) hardly changes the profile of the sorbent. Two main differences are observed at  $1714\text{ cm}^{-1}$  and  $1241\text{ cm}^{-1}$  (where the weak bands disappear); these bands are assigned to  $\nu_s(\text{C}=\text{O})$  in ester carbonyl groups and  $\nu_s(\text{C}=\text{O})$  [47] (or  $\nu(\text{C}-\text{N})$  in secondary aromatic amine, [47]).

The interaction of MB induces specific variations in the FTIR spectrum of the sorbent. The shift of the broadband at  $3310\text{ cm}^{-1}$  to  $3391\text{ cm}^{-1}$  may be caused by the sorption of MB that bears numerous N-based functional groups; the band is assigned to  $\nu_{\text{OHbond}}(\text{N}\cdots\text{H}-\text{O})$  and  $\nu_{\text{OHbond}}(\text{N}^+\cdots\text{H}-\text{O})$  [68]. The band associated with the carboxyl group ( $\nu(\text{COO}^-)$ ) is substantially changed: the intensity is decreased and superposed to the contribution of  $\nu_{\text{het}}(\text{C}=\text{N})$  and  $\nu_{\text{het}}(\text{C}=\text{C})$  bands (directly assigned to MB, [68]). In the range of  $1500\text{--}1100\text{ cm}^{-1}$ , a typical band of MB is appearing (at  $1341\text{ cm}^{-1}$ ) while the contribution of  $\nu(\text{C}-\text{N})$  (at  $1241\text{ cm}^{-1}$ ) is reduced. The bands at  $923\text{ cm}^{-1}$  ( $\nu\text{C}-\text{O}$ ) and  $850\text{ cm}^{-1}$  (PVA fingerprint) are strongly reduced and replaced with two bands at  $885\text{ cm}^{-1}$  and  $812\text{ cm}^{-1}$  (associated with MB reactive groups), respectively. The weak band at  $671\text{ cm}^{-1}$  is another marker of the presence of MB (see Table 1).

### 3.1.4. Zetametry

Fig. S3 allows determining the  $\text{pH}_{\text{PZC}}$  of the composite sorbent and its components (i.e., biochar and GG). The  $\text{pH}_{\text{PZC}}$  of the sorbent is close to 6.43, while the  $\text{pH}_{\text{PZC}}$  of the native biochar and GG are close to 6.8 and 2.3, respectively. This value is consistent with the value reported for other types of biochar (i.e.,  $6.15 \pm 0.15$  [69]). Kaur and Kaur [70] investigated the association of GG with guar gum (cationic polyelectrolyte): GG remains negatively charged on a wide pH range, and the  $\text{pK}_a$  value of the carboxylic group is close to 3.72.

### 3.1.5. Contact angle

The contact angle was measured by the water drop procedure on the sorbent before MB sorption (Fig. S4). The value is close to  $88.6 \pm 0.7^\circ$ . This value is much higher than the data reported by Vashisth and Pruthi [71] for raw GG/PVA nanofibers. Aadil et al. [72] also reported a much lower contact angle (meaning higher hydrophilicity) for GG/PVA nanofibers (i.e., close to  $35^\circ$ ). However, Vashisth and Pruthi [71] also observed that by playing with the crosslinking post-treatment, the

**Table 1**

FTIR assignments for main bands on sorbent (raw), conditioned sorbent (after pH control), and after MB sorption.

Assignment	Sorbent	Sorbent (pH)	Sorbent + MB	Reference
$\nu(\text{OH}), \nu_{\text{OHbond}}(\text{N}\cdots\text{H}-\text{O}), \nu_{\text{OHbond}}(\text{N}^+\cdots\text{H}-\text{O})$	3310	3310	3391	[68,72]
$\nu(-\text{CH}_2)$	2937	2937	2938	[68]
$\nu_s(\text{CH}_3)$	2881	2881		[68]
$\nu_s(\text{C}=\text{O})$ (ester carbonyl group)		1714		[47]
$\nu_{\text{as}}(\text{COO}^-)$	1653	1653		[72]
$\nu_{\text{het}}(\text{C}=\text{N}), \nu_{\text{het}}(\text{C}=\text{C})$			1604	[68]
$\nu_{\text{het}}(\text{C}=\text{S}^+)$			1491	[68]
$\nu(-\text{CH}_2)$	1419	1419		[72,102]
$\delta(\text{CH}_3)$			1398	[68]
$\nu_{\text{het}}(\text{C}=\text{S}^+)$ and/or $\nu(\text{CN})$ (in $\text{NCH}_3$ )			1341	[68]
$\nu(\text{C}-\text{N})$	1241	1213		[47]
$\nu(\text{C}-\text{O}), \nu(\text{C}-\text{O}-\text{C})$	1107	1107	1103	[47]
$\nu(\text{C}-\text{O}), \nu_{\text{het}}(\text{C}-\text{H})$	1034	1034	1042	[68,72,102]
Carbohydrate fingerprint	994	994		[103]
$\nu(\text{C}-\text{O})$ (alkyl ether)	923	923		[47]
$\gamma_{\text{het}}(\text{C}-\text{H})$			885	[68]
PVA fingerprint	850	850		[102]
$\delta_{\text{het}}(\text{C}-\text{C})$			812	[68]
$\nu_s(\text{C}-\text{S}-\text{C}) + \nu(\text{C}-\text{N}) + \delta(\text{C}-\text{H})$ in-plane, $\delta(\text{C}-\text{H})$ bending out-of-plane, $\delta(\text{C}-\text{S}-\text{C}), \delta_{\text{heterocycle}}(\text{C}-\text{C})$			671	[68]

contact angle may increase from  $30^\circ$  to  $81^\circ$ . Probably, this specific film-forming method (including glycerol and drying/casting steps) contributes to increased hydrophobicity.

After MB sorption, it was not possible to report accurate values of the contact angle: the water drop is immediately absorbed making difficult the measurement of the angle.

## 3.2. Sorption studies

### 3.2.1. Effect of pH on MB sorption

Fig. 4 shows the effect of equilibrium  $\text{pH}_{\text{eq}}$  on the sorption of MB using the composite sorbent. The sorption efficiency continuously increases with the pH. Below  $\text{pH}_{\text{PZC}}$ , the steepness of the curve is stronger than above pH 6.4. Methylene blue is a cationic dye; the equal distribution between  $\text{MB}^+$  and  $\text{MB}^0$  is reached at  $\text{pH} = \text{pK}_a = 3.8$  [73]. The positive charge of the sorbent below pH 6.4 causes repulsion of MB molecules in acidic solutions; increasing the  $\text{pH}_0$  from 1.6 to 10.5

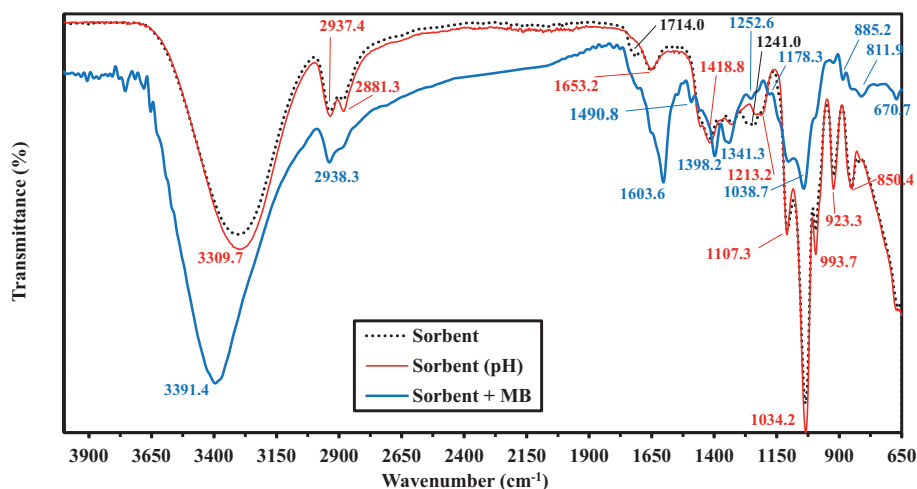


**Fig. 3.** FTIR spectra of Sorbent: as-produced, after being in contact with water at controlled pH (corresponding to MB sorption), and after MB (sorption) (SD:  $0.3\text{ g L}^{-1}$ ;  $C_0$ :  $0.3\text{ mmol MB L}^{-1}$ ;  $\text{pH}_0$ : 10.5).

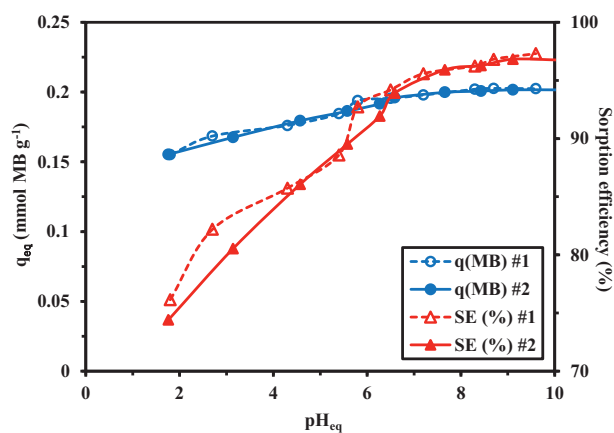


Fig. 4. Effect of pH on MB sorption ( $C_0$ : 0.3 mmol MB L<sup>-1</sup>; Sorbent dose, SD: 1.5 g L<sup>-1</sup>; time: 150 min; v: 200 rpm; T: 25 °C; duplicate series).

reduces the repulsion and the sorption capacity progressively increases from 0.155 to 0.202 mmol MB g<sup>-1</sup>.

It is noteworthy that, under strongly acidic conditions (pH 1.6–1.8), there is an appreciable amount of dye that was sorbed into sorbent particles. Under these conditions, the dye molecules as well as the sorbent are protonated. This means that the binding of the dye also involves interactions different from electrostatic attraction; probably associated with electron donor-acceptor interactions; hence, Tran et al. [74] discussed the mechanisms involved in methylene green (another cationic dye) binding onto a series of hydrochars. They identified 5 different modes of interaction: (a) pore filling (negligible because of limited porous volume, contrary to the current composite), (b) electrostatic interaction (predominant), (c) n- $\pi$  interaction, (d)  $\pi$ - $\pi$  interaction, and (e) H-bonding interactions (including Yoshida H-bonding and dipole-dipole H bonding). Hoslett et al. [75] also reported the contributions of electrostatic,  $\pi$  electron donor-acceptor, and  $\pi$ - $\pi$  stacking interactions to the binding of MB onto biochar (produced by pyrolysis of mixed municipal discarded material). Ofomaja [76] reports the capacity of MB to form protonated monomeric and dimeric MB micelles that may bind to anionic and neutral palm kernel fibers, respectively. In the case of MB sorption using graphene oxide/hollow mesoporous silica composite, Yilmaz [77] identified the main contributions of electrostatic and  $\pi$ - $\pi$  stacking interactions. Al-Ghouthi and Al-Absi [78] assigned different mechanisms for MB sorption onto olive stones depending on the pH of the solution: (a) in acidic solutions MB is bound through hydrogen bonding with -OH groups of cellulose fraction, (b) in neutral solutions, hydrophobic-hydrophobic interactions are involved, while (c) in basic media, electrostatic interaction may be involved.

Fig. 5a shows that the pH remains relatively constant during sorption: the pH varies by <0.5 pH unit. The log<sub>10</sub> plot of distribution coefficient D (defines as:  $D = q_{eq}/C_{eq}$ , L g<sup>-1</sup>) vs. pH<sub>eq</sub> (Fig. 5b) shows that D linearly increases with the pH. In ion-exchange mechanisms, the slope is associated with the stoichiometric ratio of proton exchange with solute ions. Herein, the slope is close to +0.14; this is not consistent with a possible ionic ratio between MB species and reactive groups on the sorbent; as another evidence that the electrostatic attraction is not the predominant or unique mechanism involved in MB binding.

### 3.2.2. Effect of agitation speed, sorbent dose, and NaCl concentration on equilibrium sorption

The agitation speed shows a limited effect on sorption capacity (from 0.195 to 0.204 mmol MB g<sup>-1</sup>) and efficiency (from 94.4 to 97.4 %) at equilibrium (Fig. 6a). The agitation speed may influence the equilibrium time: lower agitation requires longer contact time. In these experiments, the contact time was systematically set to 150 min; this may be not enough in the case of the agitation regime; however, despite these

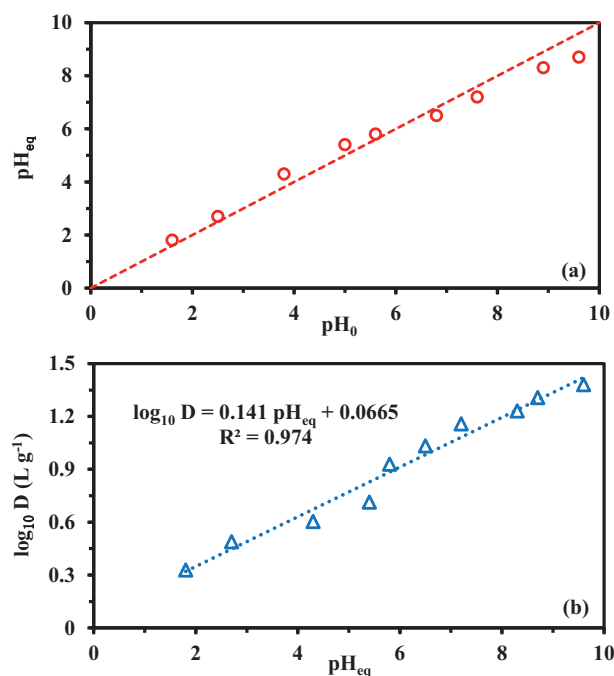


Fig. 5. Effect of pH on MB sorption: (a) pH variation, (b) log<sub>10</sub> plot of D vs. pH<sub>eq</sub> ( $C_0$ : 0.3 mmol L<sup>-1</sup>; SD: 1.5 g L<sup>-1</sup>; v: 200 rpm; time: 150 min).

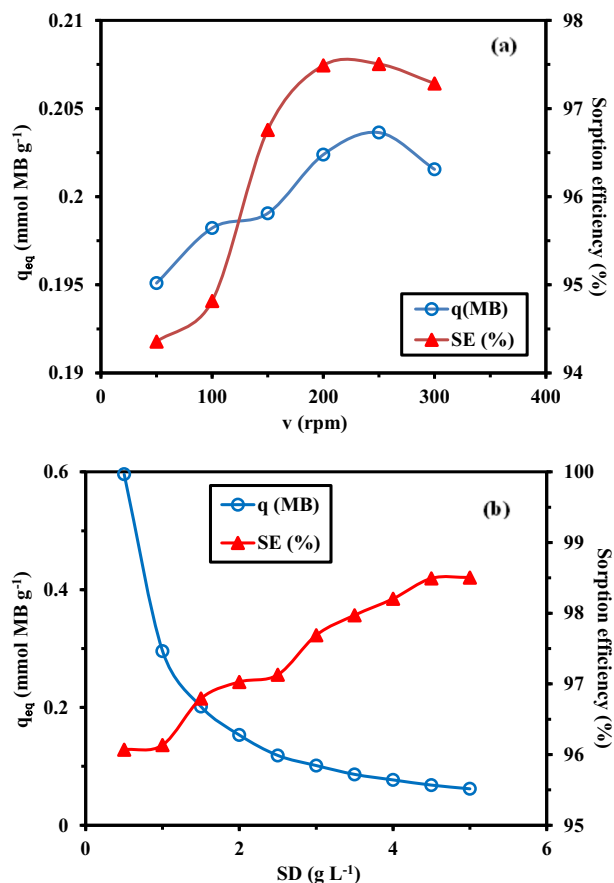


Fig. 6. (a) Effect of agitation speed on MB sorption: Sorption capacity ( $q_{eq}$ , mmol MB g<sup>-1</sup>) and sorption efficiency (%) ( $C_0$ : 0.3 mmol L<sup>-1</sup>; pH<sub>0</sub>: 10.5; SD: 1.5 g L<sup>-1</sup>; v: 50–300 rpm; time: 150 min). (b) Effect of sorbent dose on MB sorption: Sorption capacity ( $q_{eq}$ , mmol MB g<sup>-1</sup>) and sorption efficiency (%) ( $C_0$ : 0.3 mmol L<sup>-1</sup>; pH<sub>0</sub>: 10.5; SD: 0.5–5 g L<sup>-1</sup>; v: 200 rpm; time: 150 min).

unfavorable conditions, the pseudo-equilibrium performances are hardly affected by this parameter. For further experiments, the agitation is fixed to 200 rpm, which corresponds to optimum conditions. The agitation speed is supposed to play a significant role in the control of uptake kinetics through the resistance to film diffusion.

As expected, increasing sorbent dose increases sorption efficiency (Fig. 6b). However, under selected experimental conditions, the sorption efficiency hardly varies (from 96 % to 98.5 %) when the sorbent dose increases 10 times (from 0.5 to 5 g L<sup>-1</sup>). However, under these conditions, the sorption capacity is drastically reduced (from 0.596 to 0.062 mmol MB g<sup>-1</sup>). For further experiments, the standard sorbent dose was set to 1.5 g L<sup>-1</sup>, in order to maintain both high sorption efficiency and capacity.

The effluents from the dyeing industry frequently contain high concentrations of salt. This may be of critical importance because, in the case of ion-exchange mechanisms, high ionic strength may cause a dramatic decrease in sorption performance [79]. Fig. 7 shows that the addition of NaCl to the dye solution has a negligible impact on MB removal: the efficiency decreases by <8 % when NaCl concentration reaches 45 g L<sup>-1</sup>. On the other side, the sorption capacity varies by <6 % (from 0.202 to 0.190 mmol MB g<sup>-1</sup>). This weak effect of ionic strength confirms that the mechanism of electrostatic attraction is not playing the predominant role in MB sorption by the composite. In the case of MB sorption onto biochar, Ji et al. [80] observed a weak increase in sorption with increasing NaCl to 0.1 mM: they explain that NaCl enhances the protonation of the sorbent and the ionization of the dye; however, they did not investigate the impact of higher ionic strength. On the opposite hand, Alver et al. [81] recently reported a drastic decrease in MB sorption capacity onto magnetic alginate/rice husk composite when the concentration of NaCl increases (from 83 to 8 mg MB g<sup>-1</sup>, when reaching 1 % NaCl ionic strength). They assigned this strong decrease to the competitor effect of Na<sup>+</sup> ions that shield the negative charge of alginate-based material, preventing the binding of cationic MB molecules.

### 3.2.3. Uptake kinetics

The sorption kinetics may be controlled by several mechanisms associated with diffusion regimes (resistance to bulk, film, and/or intraparticle diffusion) and to the proper reaction rates. The contribution of these phenomena may be affected by parameters such as sorbate concentration, pH, temperature, agitation speed, porosity of the sorbent (especially in relation with the size of the sorbate), and so on [58].

3.2.3.1. Effect of agitation speed (mechanical agitation). Fig. 8 shows the kinetic profile for MB sorption using the composite sorbent under selected experimental conditions: under mechanical agitation, the speed

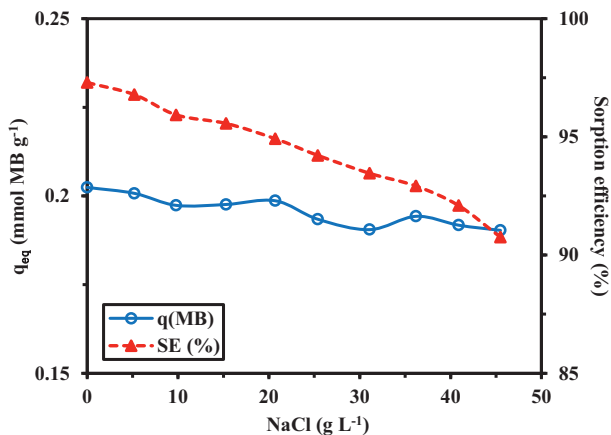


Fig. 7. Effect of NaCl concentration on MB sorption: sorption capacity ( $q_{eq}$ , mmol MB g<sup>-1</sup>) and sorption efficiency (%) ( $C_0$ : 0.3 mmol L<sup>-1</sup>; pH<sub>0</sub>: 10.5; SD: 1.5 g L<sup>-1</sup>; v: 200 rpm; time: 150 min).

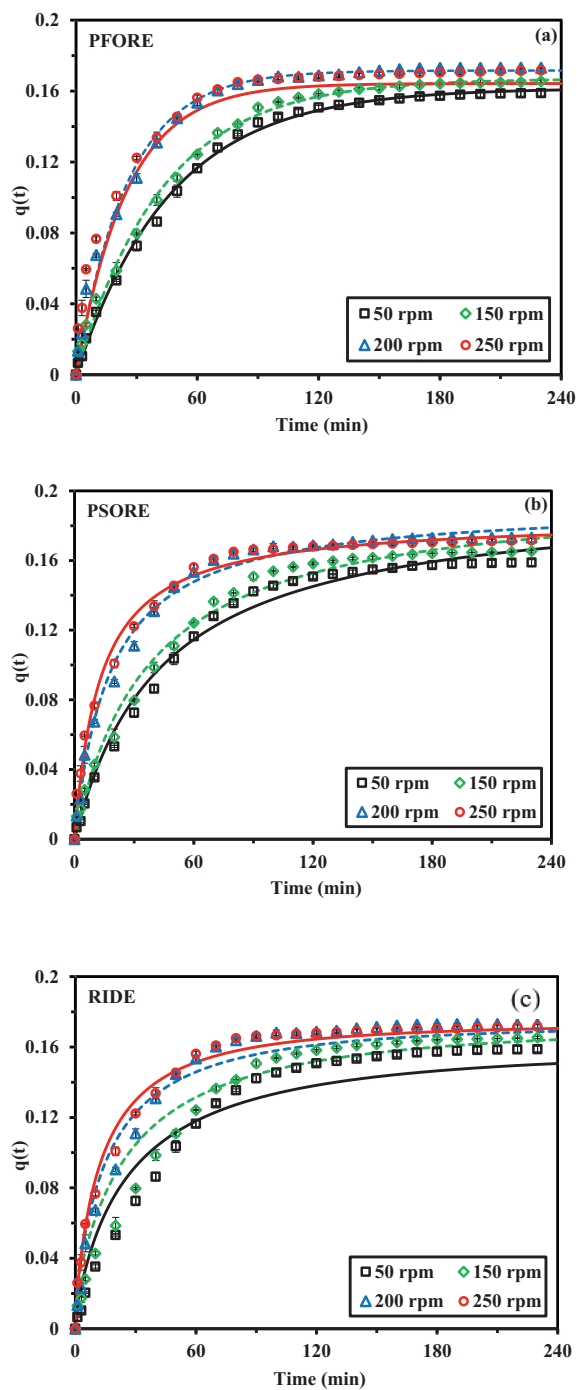


Fig. 8. Effect of agitation speed on MB uptake kinetics using composite sorbent – Modeling with (a) PFORE and (b) PSORE and (c) RIDE ( $C_0$ : 0.31 mmol MB L<sup>-1</sup>; pH<sub>0</sub>: 10.5; SD: 1.5 g L<sup>-1</sup>; v: 50–250 rpm; T: 25 °C).

was varied between 50 and 250 rpm. With an agitation speed set at 200 rpm, the contribution of resistance to bulk and film diffusion is minimized. The  $t_{50\%}$  (time required to reach half of the total sorption) varies between 30 min (at v: 50 rpm) and 18–22 min (at 200–250 rpm); the  $t_{90\%}$  decreases from 94 min to 62–68 min with increasing the agitation speed. The agitation speed is usually affecting the resistance to external diffusion and bulk diffusion playing with both the thickness of the film surrounding the particles and the homogeneity in the distribution of the solute and sorbent particles in the reactor, respectively. Above 200 rpm, the variations are not very marked, and this agitation speed sounds a good compromise. This is consistent with the preliminary tests collected

at equilibrium in Fig. 6a. The agitation speed hardly influences the sorption capacity at equilibrium:  $q_{eq,exp.}$  is close to  $0.165 \pm 0.006$  mmol MB  $g^{-1}$ .

The required contact time for reaching equilibrium is close to 180 min. This probably means that the resistance to intraparticle diffusion controls sorption kinetics, at least partially. The sorption operates through rapid sorption at the surface of the sorbent followed by slow sorption inside sorbent particles (controlled by the resistance to intraparticle diffusion). Jia et al. [82] reported the length and width of MB molecule:  $\approx 14$ , and  $9.5$ , respectively; which, is larger than the values reported for pore size (as determined by  $N_2$  adsorption/desorption isotherms on dry sorbent particles). The soaking of the sorbent (when dropped into the dye solution) may expand the porous network to make internal reactive groups more accessible and available to dye molecules. However, despite this possible expansion, the respective sizes of pores and dye molecules cause kinetic restrictions to dye transfer. Experimental points are superposed with the fitted curves for PFORE (Fig. 8a) and PSORE (Fig. 8b) while Fig. 8c shows RIDE fitting (model's equations are summarized in Table S1). Table 2 reports the parameters of the models (together with statistical criteria: determination coefficient,  $R^2$ , and Akaike Information Criterion, AIC). The quality of the fits for the different models are ranked according:

PFORE > PSORE >> RIDE

Due to the poor fit of experimental profiles by the Elovich equation, the simulated profiles are not presented. It is noteworthy that the comparison of calculated  $q_{eq}$  values with experimental values shows that the PFORE values are very close to experimental values (i.e.,  $q_{eq,exp.}$  the variation being <2 %) while the PSORE overestimates the reference value by 10–25 %. The PFORE offers a global better simulation of the kinetic profile. Dragan and Apopei Loghin [83] also report close fits of MB uptake kinetics by PFORE and PSORE when using modified starch/polyacrylamide composites. Elwakeel et al. [84] obtained  $k_1$  values close to  $4.1 \times 10^{-2} \text{ min}^{-1}$ , for MB binding onto 2-mercaptobenzimidazole derivative of chitosan. Herein, the apparent rate coefficient is in the range  $2\text{--}5 \times 10^{-2} \text{ min}^{-1}$ , which is of the same order of magnitude as the values determined by Dragan and Apopei Loghin [83]. The apparent rate coefficient increases with agitation speed above 150 rpm: from  $2.11$  to  $2.26 \times 10^{-2} \text{ min}^{-1}$  at 50–150 rpm to  $3.98\text{--}4.96 \times 10^{-2} \text{ min}^{-1}$ . Recently, Chen et al. [85] reported apparent rate coefficients in the range  $0.88\text{--}1.01 \times 10^{-2} \text{ min}^{-1}$  for MB sorption onto starch-based hydrogel. Hoslett et al. [75] reported preferential kinetic modeling by the PSORE for MB binding onto char (produced from municipal wastes); the apparent rate coefficient  $k_2$  was  $3.11 \text{ g mmol}^{-1} \text{ min}^{-1}$  (about 10 times the values for the current sorbent; i.e.,  $0.12\text{--}0.42 \text{ g mmol}^{-1} \text{ min}^{-1}$ ).

The resistance to intraparticle diffusion was evaluated using the

**Table 2**  
Modeling of MB uptake kinetics – Effect of agitation speed (mechanical agitation).

Model	Parameter	Agitation speed (rpm)			
		50	150	200	250
Experimental PFORE	$q_{eq,exp}$	0.159	0.165	0.173	0.172
	$q_{eq,1}$	0.162	0.167	0.172	0.168
	$k_1 \times 10^2$	2.14	2.34	3.92	4.96
	$R^2$	0.998	0.994	0.993	0.985
PSORE	AIC	-318	-297	-283	-260
	$q_{eq,2}$	0.198	0.200	0.192	0.184
	$k_2 \times 10^2$	11.6	13.3	28.7	41.7
	$R^2$	0.991	0.988	0.992	0.989
RIDE	AIC	-280	-277	-286	-284
	$D_e \times 10^{13}$	1.09	0.716	1.18	2.09
	$R^2$	0.981	0.975	0.991	0.989
	AIC	-236	-222	-219	-215

Units:  $q_{eq}$ , mmol  $g^{-1}$ ;  $k_1$ ,  $min^{-1}$ ;  $k_2$ ,  $g \text{ mmol}^{-1} \text{ min}^{-1}$ ;  $D_e$ ,  $m^2 \text{ min}^{-1}$ .

Crank equation [86], under simplifying hypotheses such as (a) separating the contribution of this diffusion mode to the resistance to film diffusion, and (b) not taking into account the equilibrium conditions (i.e., the Langmuir or alternative equation). The application of the Crank equation supposed the sorbent to be initially free of the solute (meaning not infinite and that the concentration of the solute varies). In his reference book (The Mathematics of Diffusion), Crank defined different equations for simulating the transfer of solute within solid materials under different conditions such as finite/infinite volume, and shape of the material. Herein, the equation used for modeling kinetic profiles is based on finite volume conditions, and sorbent particles assimilated to spherical particles. This is a very simplified approach but closer to the reality of equations such as the multi-stage Weber and Morris equation [87]. This is mainly used to (a) evaluate the order of magnitude of the effective diffusion coefficient ( $D_e$ ,  $m^2 \text{ min}^{-1}$ ), (b) compare with the free diffusivity of the solute in the solvent, and (c) compare the diffusion characteristics of different materials or different solutes (under similar conditions). The Crank equation globally fits the experimental profile (Fig. 8c), though less accurately in the most curved section of the kinetic profile, and less precisely than PFORE and PSORE (as confirmed by statistical criteria in Table 2). However, this model can be used for approaching the effective diffusivity coefficient  $D_e$  (defined in Table S1): varying in the range  $0.7\text{--}2.1 \times 10^{-13} \text{ m}^2 \text{ min}^{-1}$ . Selifonov et al. [88] reported the diffusivity coefficient of MB in water, which is close to  $4.04 \times 10^{-8} \text{ m}^2 \text{ min}^{-1}$ . They observed a little decrease in  $D_e$  value considering the diffusion of dye micelle (at  $1.16 \times 10^{-8} \text{ m}^2 \text{ min}^{-1}$ ). Least [89] provided slightly higher values for the diffusivity coefficient of MB in water (i.e.,  $5.0 \times 10^{-8} \text{ m}^2 \text{ min}^{-1}$ ); he also reported the decrease in the diffusivity properties with dye aggregation (i.e., down to  $3.8 \times 10^{-8} \text{ m}^2 \text{ min}^{-1}$ ) and in the presence of counter ions (which can be bound; this is the case with NaCl). The effective diffusivity coefficient calculated from Fig. 8c (in Table 2) is thus several orders of magnitude lower than the free diffusivity of MB in water; meaning that the resistance to intraparticle diffusion takes part in the overall control of dye transfer.

**3.2.3.2. Effect of frequency (ultrasonic treatment).** Several studies have previously illustrated the benefit of using the ultrasonic treatment for improving the sorption performances of solutes [90], including dyes MB [91]. In the case of the sorption of titan yellow and rose bengal onto a magnetic metal-oxide organic framework, the application of ultrasonic treatment allowed reducing ten times the equilibrium time [92]. Herein, the  $t_{50\%}$  was reduced to 4 and 3 min ( $t_{90\%}$  to 30 and 20 min) with ultrasonic treatment; increasing the frequency ( $F$ , kHz) significantly enhances the uptake kinetics. The equilibrium sorption capacity is weakly affected by the frequency (Table 3):  $q_{eq,exp.}$  close to  $0.192\text{--}0.195$  mmol MB  $g^{-1}$  under selected experimental conditions; this is consistent with the conclusions raised by Rajumon et al. [91] in the case of MB sorption using reduced graphene oxide. The ultrasonic treatment increases the

**Table 3**  
Modeling of MB uptake kinetics – Effect of frequency (ultrasonic agitation).

Model	Parameter	Ultrasonic frequency (kHz)	
		37	80
Experimental PFORE	$q_{eq,exp}$	0.192	0.195
	$q_{eq,1}$	0.185	0.189
	$k_1 \times 10^2$	13.5	19.3
	$R^2$	0.984	0.990
PSORE	AIC	-119	-126
	$q_{eq,2}$	0.205	0.205
	$k_2 \times 10^2$	85.8	130.8
	$R^2$	0.998	0.999
RIDE	AIC	-150	-158
	$D_e \times 10^{13}$	6.57	6.66
	$R^2$	0.949	0.892
	AIC	-85	-81

Units:  $q_{eq}$ , mmol  $g^{-1}$ ;  $k_1$ ,  $min^{-1}$ ;  $k_2$ ,  $g \text{ mmol}^{-1} \text{ min}^{-1}$ ;  $D_e$ ,  $m^2 \text{ min}^{-1}$ .

equilibrium sorption capacity by about 18 %. However, the most significant impact is associated with the apparent rate coefficient that drastically increases with ultrasonic agitation, especially at higher frequency. It is noteworthy that the ultrasonic treatment also changes the modeling of the kinetic profiles: contrary to mechanical agitation, the models can be ranked according to:

PSORE > PFORE >> RIDE

In Fig. 9, the solid lines represent the fitting of experimental curves with the PSORE (using the parameters summarized in Table 3). The pseudo second order rate equation fits better the uptake kinetics under sonochemical treatment: the calculated equilibrium sorption capacity overestimates the experimental value by 6–7 %. The apparent rate coefficient  $k_2$  increases by 3 times at F: 37 kHz and up to 4.6 times at F: 80 kHz (almost the same ratios can be reported for the variation on  $k_1$  values). The beneficial effect of high frequency has been explained by its effect on the reduction of the cavitation bubbles generated during ultrasonic treatment [93]. During the collapse of cavitation bubbles, stronger microjets are formed that make more efficient the mechanical stress on the surface of the sorbent: the mass transfer is favored. This conclusion corroborates with the increase in the approximated value of the effective diffusion coefficient (up to  $6.7\text{--}8.7 \times 10^{-13} \text{ m}^2 \text{ min}^{-1}$ ). The sonication of the solution improves the equilibrium performance and even more the mass transfer and reaction rate.

### 3.2.4. Sorption isotherms and thermodynamics

Fig. S5 compares the sorption isotherms for the biochar/GG/PVA composite with the isotherms for precursors GG/PVA and biochar. The profiles clearly demonstrate the superiority of the composite sorbent that exhibits higher sorption capacity at saturation (i.e., 1.7 vs. 1.46 and 0.53 mmol MB  $\text{g}^{-1}$  for composite, biochar, and GG, respectively). However, the composite sorbent also shows a much higher affinity for MB as shown by the initial slope of the isotherm curves. Hence, the limit residual concentrations for reaching the saturation plateau corresponds to 0.2, 1.4, and 2.9 mmol MB  $\text{L}^{-1}$  for composite, GG, and biochar, respectively. This figure clearly demonstrates the synergistic effect of the association of the different precursors.

The sorption isotherms are reported in Fig. 9, at different temperatures. The good overlapping of the duplicated experimental curves confirms the reproducibility of sorption tests. The profiles are characterized by a saturation plateau reached for residual concentration close to  $C_{\text{eq}}$ : 0.2 mmol MB  $\text{L}^{-1}$  and a steep initial slope, which confirms the good affinity of the sorbent for MB. The maximum sorption capacity

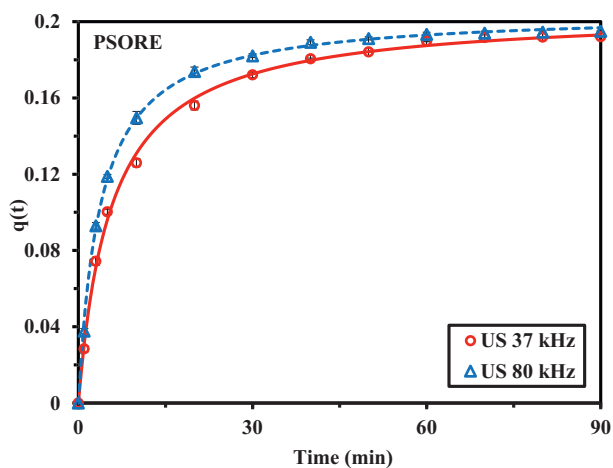


Fig. 9. MB uptake kinetics – Modeling of sorption capacity vs. time for MB sorption for different frequencies of ultrasonic agitation (kHz) using the pseudo-second order rate equation ( $C_0$ : 0.31 mmol MB  $\text{L}^{-1}$ ;  $\text{pH}_0$ : 10.5, SD: 1.5  $\text{g L}^{-1}$ ;  $v$ : 200 rpm; T: 25 °C).

ranges between 1.68 and 1.84 mmol MB  $\text{g}^{-1}$  (Table 4). Fig. S6 compares the modeling of the experimental profiles (as an example, for T: 25 °C) with the different models reported in Table S2. The asymptotic shape of the isotherm is not consistent with the exponential form of the Freundlich equation (Fig. S6a). The Temkin equation fails to fit the experimental profile at high residual concentrations and the models the most appropriate are reported in Fig. S6b. Table 4 confirms these trends. The comparison of  $R^2$  and AIC values confirms that fitting quality follows:

Sips > Langmuir > Dubinin – Radushkevich

Langmuir equation assumes the sorption to occur through monolayer coverage, without interactions between sorbed molecules and with a homogeneous distribution of sorption energies. The Sips equation was developed to simulate adsorption in heterogeneous systems and get beyond the limitation of the rising sorbate concentration associated with the Freundlich isotherm. It is a kind of combination of the Langmuir and Freundlich equations. It reduces to the Freundlich isotherm at low sorbate concentrations but predicts monolayer sorption similarly to the Langmuir isotherm at high sorbate concentrations [94]. Therefore, the Sips isotherm shall be used to describe only monolayer adsorption systems; mathematical fit is usually improved due to the introduction of a third-adjustable parameter but with less physicochemical meaning regarding sorption mechanisms. The Dubinin-Radushkevich equation was designed for modeling the sorption of gases onto microporous sorbents: the sorption occurs by pore filling rather than by covering of internal macroporous or superficial surface (for nonporous sorbents) (as in the Langmuir or Brunauer-Emmett-Teller equations). Puccia and Avelina [60] recently questioned the application of this model for solid/liquid sorption systems (especially for the interpretation and discrimination between physical and chemical sorption). Herein, the  $E_{\text{DR}}$  values tend to increase with temperature (in the range of 8.48–10.4  $\text{kJ mol}^{-1}$ ), while the Temkin energy hardly varies between 4.96 and 5.9  $\text{kJ mol}^{-1}$ .

The fitting of sorption isotherms with the Sips equation is shown in Fig. S7. In Fig. 10, the solid lines represent the fitting of experimental profiles with the Langmuir equation (using the parameters reported in Table 4). The calculated maximum sorption capacities (i.e.,  $q_{\text{m,L}}$ ) systematically overestimate experimental data (by about 10 %). Both the maximum sorption capacities and the affinity coefficients slightly increase with the temperature: the sorption is weakly endothermic. The application of the van' Hoff equation allows calculating the thermodynamic parameters (Fig. S8 and Table 5). The positive value of the enthalpy change ( $\Delta H^\circ$ :  $\approx 12.9 \text{ kJ mol}^{-1}$ ) confirms the endothermic behavior of MB sorption onto the composite sorbent. The sorption is followed by increased randomness of the system as indicated by the positive value of the entropy change ( $\Delta S^\circ$ :  $\approx 125 \text{ J mol}^{-1} \text{ K}^{-1}$ ). The negative value of the Gibbs free energy change ( $\Delta G^\circ$ : varying between  $-24.5$  and  $-28.2 \text{ kJ mol}^{-1}$ ) confirms the spontaneity of the reaction; the slight increase (absolute value) is consistent with the slight improvement of sorption performance with temperature increase. In the case of MB sorption onto olive stones, Al-Gouthi and Al-Absi [78] reported the same order of magnitude for  $\Delta G^\circ$ , while the values for  $\Delta H^\circ$  and  $\Delta S^\circ$  were substantially higher (i.e., 72  $\text{kJ mol}^{-1}$  and 297  $\text{J K}^{-1} \text{ mol}^{-1}$ , respectively). On the opposite hand, Andrade Siqueira et al. [95] reported MB endothermic sorption onto sugarcane bagasse, with lower thermodynamic values ( $\Delta H^\circ$ : 1.93  $\text{kJ mol}^{-1}$  and  $\Delta S^\circ$ : 66  $\text{J K}^{-1} \text{ mol}^{-1}$ ). In the case of MB sorption onto biochar, Ji et al. [80] reported values as high as  $\Delta H^\circ$ : 42.5  $\text{kJ mol}^{-1}$  and  $\Delta S^\circ$ : 242  $\text{J K}^{-1} \text{ mol}^{-1}$ . Amin et al. [96] compare the thermodynamic characteristics of biochar produced from banana and orange peel and observed significant variations in the enthalpy change ( $\Delta H^\circ$ : 8.7 and 18.8  $\text{kJ mol}^{-1}$ , respectively).

The MB sorption properties of composite sorbent (and precursors) are compared in Table S3 with a selection of sorbents covering activated carbon-based materials, resins, biosorbents. Recently, Chen et al. [85] designed a new sorbent with outstanding sorption properties (i.e.,  $q_{\text{m,L}}$ : superior to 8 mmol MB  $\text{g}^{-1}$ ) at a comparable pH value to the pH selected

**Table 4**  
Fitting of sorption isotherms – Parameters of the models.

Model	Temperature series #	25 °C		35 °C		45 °C		55 °C		
		1	2	1	2	1	2	1	2	
Exper.	q <sub>m</sub>	1.695	1.694	1.680	1.705	1.715	1.740	1.809	1.839	
Langmuir	q <sub>m,L</sub>	1.926	1.958	1.887	1.935	1.868	1.924	2.030	2.042	
	b <sub>L</sub>	22.2	18.4	21.9	21.8	27.2	24.7	33.6	31.4	
	R <sup>2</sup>	0.995	0.995	0.989	0.992	0.994	0.996	0.984	0.996	
	AIC	-128	-130	-113	-119	-126	-133	-101	-128	
Freundlich	k <sub>F</sub>	2.58	2.56	2.46	2.56	2.55	2.68	3.15	3.23	
	n <sub>F</sub>	2.60	2.53	2.67	2.62	2.69	2.60	2.60	2.51	
	R <sup>2</sup>	0.904	0.914	0.911	0.906	0.913	0.922	0.883	0.913	
	AIC	-65	-67	-67	-65	-67	-69	-59	-65	
Sips	q <sub>m,S</sub>	1.819	1.861	1.799	1.824	1.780	1.856	1.847	1.909	
	b <sub>S</sub>	42.9	31.2	39.7	45.8	51.1	36.7	120.7	69.8	
	n <sub>S</sub>	0.864	0.883	0.872	0.843	0.875	0.918	0.789	0.856	
	R <sup>2</sup>	0.997	0.997	0.991	0.995	0.996	0.997	0.988	0.998	
AIC		-138	-135	-113	-123	-130	-134	-105	-140	
	A <sub>T</sub>	663.8	591.3	904.3	761.6	986.3	987.4	918.4	970.4	
	b <sub>T</sub>	8681	8602	9910	9307	10,094	10,035	8966	9209	
	E <sub>T</sub>	5.12	5.09	5.90	5.46	5.89	5.77	4.96	5.01	
Temkin	R <sup>2</sup>	0.907	0.917	0.891	0.898	0.893	0.884	0.889	0.891	
	AIC	-67	-70	-64	-65	-64	-62	-62	-62	
	D-R	q <sub>m,DR</sub>	2.019	2.011	1.955	2.013	1.981	2.034	2.252	2.246
		K <sub>DR</sub> × 10 <sup>8</sup>	1.298	1.390	1.192	1.208	1.042	1.084	0.932	0.952
E <sub>DR</sub>		8.78	8.48	9.16	9.10	9.80	9.61	10.4	10.2	
R <sup>2</sup>		0.988	0.991	0.984	0.985	0.986	0.990	0.970	0.985	
AIC		-109	-116	-104	-105	-107	-114	-88	-103	

Units - q<sub>m</sub> (mmol g<sup>-1</sup>); b<sub>L</sub> (L mmol<sup>-1</sup>); k<sub>F</sub> (mmol g<sup>-1</sup>)/(mmol L<sup>-1</sup>)<sup>n<sub>F</sub></sup>, n (dimensionless); b<sub>S</sub> ((mmol L<sup>-1</sup>)<sup>n<sub>S</sub></sup>); b<sub>T</sub> (J kg mol<sup>-2</sup>); A<sub>T</sub> (L mol<sup>-1</sup>); E (kJ mol<sup>-1</sup>) is correlated to the DR constant: K<sub>DR</sub> = 1/E<sup>2</sup>.

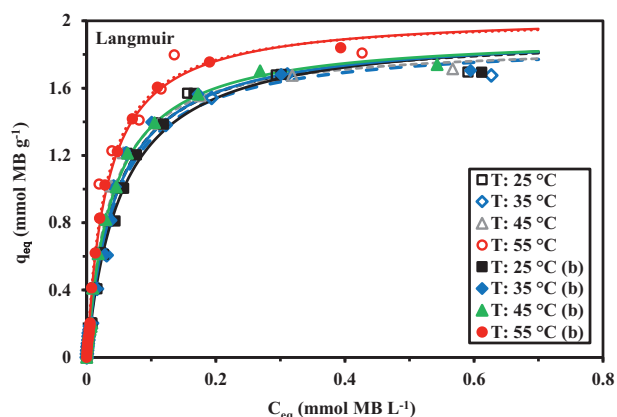


**Fig. 10.** MB sorption isotherms at pH<sub>0</sub> 10.5 at different temperatures – Langmuir modeling (C<sub>0</sub>: 0.03–3 mmol MB L<sup>-1</sup>; pH<sub>0</sub>: 10.5, SD: 1.5 g L<sup>-1</sup>; v: 200 rpm; T: 25–55 °C; time: 150 min; duplicate experiments).

**Table 5**  
Thermodynamic parameters for the sorption of MB (based on Langmuir constants).

Temperature (°C)	ΔH° (kJ mol <sup>-1</sup> )	ΔS° (J mol <sup>-1</sup> K <sup>-1</sup> )	ΔG° (kJ mol <sup>-1</sup> )
25	12.89	125	-24.47
35			-25.72
45			-26.98
55			-28.23

in this study. Magnetic polystyrene-sulfonate/chitosan [97], mesoporous activated carbon [98], activated carbon/alginate [99], and functionalized starch/polyacrylamide hydrogel [83] show also sorption capacities in the range 2–2.7 mmol MB g<sup>-1</sup>. The composite sorbent with a maximum sorption capacity of 1.93 is one of the most performing sorbents, just coming after these highly performant sorbents. It is noteworthy that the sorption capacities are much higher than those

reported for synthetic commercial resins (in the range 0.01–0.3 mmol MB g<sup>-1</sup>, [100,101]). However, the affinity coefficients are generally less favorable than alternative sorbents; this drawback is compensated by relatively fast kinetics. The sorbent has globally good and competitive sorption properties, as a compromise between sorption capacity and affinity, and kinetics.

### 3.2.5. Dye desorption and sorbent recycling

The sorption of MB being optimal in an alkaline solution, an acidic solution was selected for processing dye desorption; 0.7 M HCl solution was used for establishing desorption kinetics and testing sorbent recycling. Fig. 11 shows that the desorption proceeds within the first 60 min of contact with a desorption yield that reaches about 97 %. The first linear section of the curve (until 35–40 min) is followed by a slower desorption phase that probably corresponds to the progressive release of the dye bound in the internal porous network (which is hindered by steric hindrance). It is noteworthy that the presence of a high concentration of Cl<sup>-</sup> in the eluent is supposed to enhance the self-aggregation of MB [89], which, in turn, is expected to decrease the diffusivity of MB. A

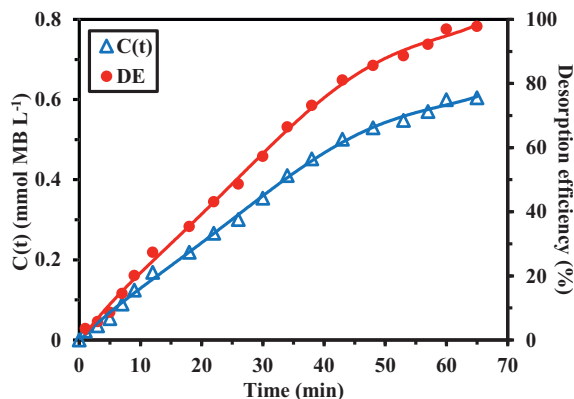


**Fig. 11.** MB desorption kinetics from dye-loaded composite sorbent using 0.7 M HCl solution (q<sub>0</sub>: 0.206 mmol MB g<sup>-1</sup>; SD: 3 g L<sup>-1</sup>; v: 200 rpm; T: 25 °C).

contrary trend is apparently observed; indeed, the desorption step is globally faster than the sorption stage.

Based on the high yield of desorption while using 0.7 M HCl solutions, this eluent was selected for comparing MB sorption and desorption efficiencies for six successive sorption/desorption cycles (with demineralized washing step between each operation). Table 6 shows the progressive decrease of the sorption capacity; however, in the sixth cycle, the loss remains below 5 % (compared with the first step). This is of the same order that the diminution of desorption efficiency, which decreases from 96.5 to 90.1 %: the cumulative desorption efficiency reaches 94 % in the sixth cycle. These results demonstrate the remarkable stability of sorption and desorption performances.

### 3.2.6. Application to MB-spiked wastewater

Wastewater was collected from the effluent of a local dyeing facility, in the industrial zone of Port Said, Egypt. The sample was spiked with MB at the concentration of 20.0 mg MB L<sup>-1</sup> (i.e., 0.0625 mmol MB L<sup>-1</sup>). The pH of the effluent was 6.7 (original pH). The conductivity was 870 μS cm<sup>-1</sup> using a conductivity meter (4510 Bench Conductivity Meter, JENWAY, UK), while the color and the COD (Chemical oxygen demand) were 998 NTU and 242 mg O<sub>2</sub> L<sup>-1</sup>, respectively, the analysis was performed using Hi 83,214 wastewater treatment photometer (HANNA instrument, USA). Fig. 12 shows the decay curves for COD and NTU with increasing sorbent dose. The composite sorbent strongly decolorizes the effluent by about 97 % with 1 g L<sup>-1</sup> sorbent dose (increasing SD does not significantly the efficiency of color loss). The COD is also reduced; however, the decrease is more progressive and incomplete: the sorbent dose may be as high as 3 g L<sup>-1</sup> for reaching the plateau of COD abatement (which does not exceed 62 %). A fraction of the organic contaminants remains refractory to the sorption treatment.

## 4. Conclusion

The comparison of sorption performances for GG/PVA and biochar with those of composite material clearly demonstrates the synergistic effect of precursors. The incorporation of the biochar (produced from a local Egyptian plant) in the composite allows for producing an efficient sorbent. The deprotonation of the sorbent in alkaline solutions improves the sorption of Methylene Blue which reaches a maximum close to pH 10.5. The fitting of sorption isotherms at different temperatures with the Langmuir equation allows calculating the enthalpy and the entropy change, which confirm the endothermic nature of MB binding onto the composite. The agitation speed influences uptake kinetics (with optimum conditions close to 200 rpm); however, alternative mode of agitation such as sonication allows drastically reducing the equilibrium time: the cavitation effects initiated by ultrasonic treatment enhance mass transfer properties (accessibility) and sorption capacities (availability of reactive groups). Applying sonication involves the reversal of fitting of experimental curves with pseudo-second order rate equation instead of the pseudo-first order rate equation. The sorption properties are remarkably maintained even in the presence of a large excess of NaCl, while the acidic desorption of the dyes allows minimized loss in sorption/desorption performance after six cycles. This bio-based material shows outstanding properties for the treatment of colored complex effluent (as confirmed by the efficiency in color removal of MB-spiked industrial effluent).

### CRedit authorship contribution statement

**Ahmed M. Elgarahy:** Conceptualization, Methodology, Investigation, Data curation.

**Hamida Y. Mostafa:** Conceptualization, Methodology, Investigation, Data curation.

**Elsayed G. Zaki:** Methodology, Investigation, Data curation.

**Shymaa M. Elsaheed:** Methodology, Investigation, Data curation.

**Khalid Z. Elwakeel:** Methodology, Investigation, Data curation.

**Table 6**

Sorbent recycling: sorption capacity and desorption efficiency (for 6 cycles).

Cycle	Sorption capacity (q <sub>eq</sub> , mmol g <sup>-1</sup> )	Desorption efficiency (%)
#1	0.207	96.5
#2	0.206	96.0
#3	0.205	95.1
#4	0.203	93.6
#5	0.199	92.5
#6	0.197	90.1
Loss at 6th/1st cycle: -4.8 %		Cumul. Desorption at 6th Cycle: 94.0 %

Experimental conditions – Sorption: C<sub>0</sub>: 0.32 mmol MB L<sup>-1</sup>; pH<sub>0</sub>: 10.5; SD: 1.5 g L<sup>-1</sup>; time: 65 min; v: 200 rpm/Desorption: Eluent: 0.7 M HCl; SD: 3 g L<sup>-1</sup>; time: 65 min; v: 200 rpm).

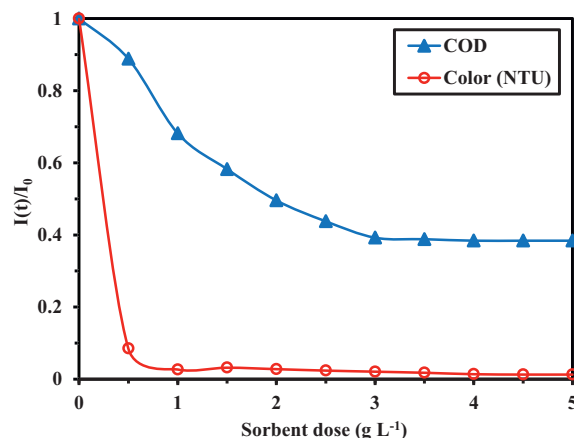


**Fig. 12.** Effect of sorbent dose on the treatment of industrial wastewater – COD and Color abatements (pH<sub>0</sub>: 6.7; time: 150 min; v: 200 rpm).

**Abdullah Akhdhar:** Methodology, Investigation.

**Eric Guibal:** Conceptualization, Review, Data curation, writing and Editing

### Declaration of competing interest

The authors declare that they have no known competing financial interests or personal relationships that could have appeared to influence the work reported in this paper.

### Data availability

Data will be made available on request.

### Acknowledgments

Authors thanks Dr. M.G. Eloffy for technical assistance.

### Appendix A. Supplementary data

Supplementary data to this article can be found online at <https://doi.org/10.1016/j.ijbiomac.2023.123355>.

### References

- [1] G. Han, Y. Du, Y. Huang, W. Wang, S. Su, B. Liu, Study on the removal of hazardous Congo red from aqueous solutions by chelation flocculation and precipitation flotation process, *Chemosphere* 289 (2022), 133109, <https://doi.org/10.1016/j.chemosphere.2021.133109>.
- [2] Y. Li, Y. An, R. Zhao, Y. Zhong, S. Long, J. Yang, J. Li, H. Zheng, Synergetic removal of oppositely charged dyes by co-precipitation and amphoteric self-floating capturer: mechanism investigation by molecular simulation,

- Chemosphere 296 (2022), 134033, <https://doi.org/10.1016/j.chemosphere.2022.134033>.
- [3] M. Liu, W. Yin, T.-L. Zhao, Q.-Z. Yao, S.-Q. Fu, G.-T. Zhou, High-efficient removal of organic dyes from model wastewater using Mg(OH)<sub>2</sub>-MnO<sub>2</sub> nanocomposite: synergistic effects of adsorption, precipitation, and photodegradation, *Sep. Purif. Technol.* 272 (2021), 118901, <https://doi.org/10.1016/j.seppur.2021.118901>.
- [4] L.V. Blanco, O.G. Sas, P.B. Sanchez, A.D. Santiago, B.G. de Prado, Congo red recovery from water using green extraction solvents, *Water Resour. Ind.* 27 (2022), 100170, <https://doi.org/10.1016/j.wri.2021.100170>.
- [5] L. Bukman, V.R. De Souza, N.R. Camargo Fernandes, W. Caetano, V.R. Batistela, N. Hioka, Reverse micellar extraction of dyes based on fatty acids and recoverable organic solvents, *Sep. Purif. Technol.* 242 (2020), 116772, <https://doi.org/10.1016/j.seppur.2020.116772>.
- [6] S. Yi, G. Sun, F. Dai, Removal and separation of mixed ionic dyes by solvent extraction, *Text. Res. J.* 88 (14) (2018) 1641–1649, <https://doi.org/10.1177/0040517517705631>.
- [7] J. Ma, J. Zhang, D. Li, Removal of methylene blue by lava adsorption and catalysis oxidation, *Environ. Technol.* 31 (3) (2010) 267–276, <https://doi.org/10.1080/09593330903453244>.
- [8] Y. Wang, W. Zhang, M. Qin, M. Zhao, Y. Zhang, Green one-pot preparation of -Fe<sub>2</sub>O<sub>3</sub>@carboxyl-functionalized yeast composite with high adsorption and catalysis properties for removal of methylene blue, *Surf. Interface Anal.* 50 (3) (2018) 311–320, <https://doi.org/10.1002/sia.6370>.
- [9] O. Dlugosz, A. Staron, P. Brzosa, M. Banach, Synergistic effect of sorption and photocatalysis on the degree of dye removal in single and multicomponent systems on ZnO-SnO<sub>2</sub>, *Environ. Sci. Pollut. Res.* 29 (2022) 27042–27050, <https://doi.org/10.1007/s11356-021-18044-7>.
- [10] R.H. Thabet, M.K. Fouad, I.A. Ali, S.A. El Sherbiny, M.A. Tony, Synthesis, characterization and potential application of magnetized nanoparticles for photocatalysis of levafix CA reactive azo-dye in aqueous effluent, *Water Environ. J.* 36 (2) (2021) 245–260, <https://doi.org/10.1111/wej.12756>.
- [11] M. Anpo, T. Shima, S. Kodama, Y. Kubokawa, Photocatalytic hydrogenation of CH<sub>3</sub>CCH with H<sub>2</sub>O on small-particle TiO<sub>2</sub>: size quantization effects and reaction intermediates, *J. Phys. Chem.* 91 (16) (1987) 4305–4310, <https://doi.org/10.1021/j100300a021>.
- [12] U.I. Gaya, A.H. Abdullah, Heterogeneous photocatalytic degradation of organic contaminants over titanium dioxide: a review of fundamentals, progress and problems, *J. Photochem. Photobiol. C* 9 (1) (2008) 1–12, <https://doi.org/10.1016/j.jphotochemrev.2007.12.003>.
- [13] M. Naushad, M.A. Khan, Z.A. Alotthan, M.R. Khan, M. Kumar, Adsorption of methylene blue on chemically modified pine nut shells in single and binary systems: isotherms, kinetics, and thermodynamic studies, *Desalin. Water Treat.* 57 (34) (2016) 15848–15861, <https://doi.org/10.1080/19443994.2015.1074121>.
- [14] R. Bushra, S. Mohamad, Y. Alias, Y. Jin, M. Ahmad, Current approaches and methodologies to explore the perceptive adsorption mechanism of dyes on low-cost agricultural waste: a review, *Microporous Mesoporous Mater.* 319 (2021), 111040, <https://doi.org/10.1016/j.micromeso.2021.111040>.
- [15] M.H. Beyki, S.E. Ganjbaksh, S. Minaeian, F. Shemirani, Clean approach to synthesis of graphene like CuFe<sub>2</sub>O<sub>4</sub>@polysaccharide resin nanohybrid: bifunctional compound for dye adsorption and bacterial capturing, *Carbohydr. Polym.* 174 (2017) 128–136, <https://doi.org/10.1016/j.carbpol.2017.06.056>.
- [16] W. Song, B. Gao, X. Xu, L. Xing, S. Han, P. Duan, W. Song, R. Jia, Adsorption-desorption behavior of magnetic amine/Fe<sub>3</sub>O<sub>4</sub> functionalized biopolymer resin towards anionic dyes from wastewater, *Bioresour. Technol.* 210 (2016) 123–130, <https://doi.org/10.1016/j.biortech.2016.01.078>.
- [17] A.C. Sadiq, A. Olasupo, W.S.W. Ngah, N.Y. Rahim, F.B.M. Suah, A decade development in the application of chitosan-based materials for dye adsorption: a short review, *Int. J. Biol. Macromol.* 191 (2021) 1151–1163, <https://doi.org/10.1016/j.ijbiomac.2021.09.179>.
- [18] C. Osagie, A. Othmani, S. Ghosh, A. Malloum, Z.K. Esfahani, S. Ahmadi, Dyes adsorption from aqueous media through the nanotechnology: a review, *J. Mater. Res. Technol.* 14 (2021) 2195–2218, <https://doi.org/10.1016/j.jmrt.2021.07.085>.
- [19] S.M. Al-Rashed, A.A. Al-Gaid, Kinetic and thermodynamic studies on the adsorption behavior of rhodamine B dye on duolite C-20 resin, *J. Saudi Chem. Soc.* 16 (2) (2012) 209–215, <https://doi.org/10.1016/j.jscs.2011.01.002>.
- [20] Y. Hu, T. Guo, X. Ye, Q. Li, M. Guo, H. Liu, Z. Wu, Dye adsorption by resins: effect of ionic strength on hydrophobic and electrostatic interactions, *Chem. Eng. J.* 228 (2013) 392–397, <https://doi.org/10.1016/j.cej.2013.04.116>.
- [21] X. Zhang, A. Li, Z. Jiang, Q. Zhang, Adsorption of dyes and phenol from water on resin adsorbents: effect of adsorbate size and pore size distribution, *J. Hazard. Mater.* 137 (2) (2006) 1115–1122, <https://doi.org/10.1016/j.jhazmat.2006.03.061>.
- [22] A.S. Pisareva, T.I. Tikhomirova, Sorption of synthetic anionic amaranth dye from an aqueous solution on hydrophobized silica and alumina, *Russ. J. Phys. Chem. A* 93 (3) (2019) 534–537, <https://doi.org/10.1134/s0036024419030142>.
- [23] Y. Lei, G. Huang, Q. Huang, J. Dou, L. Dai, F. Deng, M. Liu, X. Li, X. Zhang, Y. Wei, Facile synthesis of ionic liquid modified silica nanoparticles for fast removal of anionic organic dyes with extremely high adsorption capacity, *J. Mol. Liq.* 347 (2022), 117966, <https://doi.org/10.1016/j.molliq.2021.117966>.
- [24] M. Pishnamazi, A. Khan, T.A. Kurniawan, H. Sanaeepur, A.B. Albadarin, R. Soltani, Adsorption of dyes on multifunctionalized nano-silica KCC-1, *J. Mol. Liq.* 338 (2021), 116573, <https://doi.org/10.1016/j.molliq.2021.116573>.
- [25] N.C. Corda, M.S. Kini, A Review on Adsorption of Cationic Dyes Using Activated Carbon, *International Conference on Research in Mechanical Engineering Sciences (RiMES)*, in: INDIA, Manipal, 2017, p. 02022.
- [26] K. Zare, V.K. Gupta, O. Moradi, A.S.H. Makhlof, M. Sillanpaa, M.N. Nadagouda, H. Sadegh, R. Shahryari-Ghoshekandi, A. Pal, Z.-J. Wang, I. Tyagi, M. Kazemi, A comparative study on the basis of adsorption capacity between CNTs and activated carbon as adsorbents for removal of noxious synthetic dyes: a review, *J. Nanostruct. Chem.* 5 (2) (2015) 227–236, <https://doi.org/10.1007/s40097-015-0158-x>.
- [27] R.K. Gautam, M. Goswami, R.K. Mishra, P. Chaturvedi, M.K. Awasthi, R. S. Singh, B.S. Giri, A. Pandey, Biochar for remediation of agrochemicals and synthetic organic dyes from environmental samples: a review, *Chemosphere* 272 (2021), 129917, <https://doi.org/10.1016/j.chemosphere.2021.129917>.
- [28] S. Praveen, J. Jegan, T.B. Pushpa, R. Gokulan, L. Bulgariu, Biochar for removal of dyes in contaminated water: an overview, *Biochar* 4 (1) (2022) 10, <https://doi.org/10.1007/s42773-022-00131-8>.
- [29] P. Srivatsav, B.S. Bhargav, V. Shanmugasundaram, J. Arun, K.P. Gopinath, A. Bhatnagar, Biochar as an eco-friendly and economical adsorbent for the removal of colorants (dyes) from aqueous environment: a review, *Water* 12 (12) (2020) 3561, <https://doi.org/10.3390/w12123561>.
- [30] S. Sutar, P. Patil, J. Jadhav, Recent advances in biochar technology for textile dyes wastewater remediation: a review, *Environ. Res.* 209 (2022), 112841, <https://doi.org/10.1016/j.envres.2022.112841>.
- [31] X.-F. Tan, Y.-G. Liu, Y.-L. Gu, Y. Xu, G.-M. Zeng, X.-J. Hu, S.-B. Liu, X. Wang, S.-M. Liu, J. Li, Biochar-based nano-composites for the decontamination of wastewater: a review, *Bioresour. Technol.* 212 (2016) 318–333, <https://doi.org/10.1016/j.biortech.2016.04.093>.
- [32] Z.F. Akl, E.G. Zaki, S.M. ElSaeed, Green hydrogel-biochar composite for enhanced adsorption of uranium, *ACS Omega* 6 (50) (2021) 34193–34205, <https://doi.org/10.1021/acsomega.1c01559>.
- [33] A.I. Osman, S. Fawzy, M. Farghali, M. El-Azazy, A.M. Elgarahy, R.A. Fahim, M.I. A.A. Maksoud, A.A. Ajlan, M. Yousry, Y. Saleem, D.W. Rooney, Biochar for agronomy, animal farming, anaerobic digestion, composting, water treatment, soil remediation, construction, energy storage, and carbon sequestration: a review, *Environ. Chem. Lett.* (2022), <https://doi.org/10.1007/s10311-022-01424-x>.
- [34] T. Bandara, J. Xu, I.D. Potter, A. Franks, J.B.A.J. Chaturika, C. Tang, Mechanisms for the removal of Cd(II) and Cu(II) from aqueous solution and mine water by biochars derived from agricultural wastes, *Chemosphere* 254 (2020), 126745, <https://doi.org/10.1016/j.chemosphere.2020.126745>.
- [35] J. Dobrzyńska, A. Wysokińska, R. Olchowski, Raspberry stalks-derived biochar, magnetic biochar and urea modified magnetic biochar - synthesis, characterization and application for As(V) and Cr(VI) removal from river water, *J. Environ. Manag.* 316 (2022), 115260, <https://doi.org/10.1016/j.jenvman.2022.115260>.
- [36] Y. Qin, J. Luo, Y. Zhao, C. Yao, Y. Li, Q. An, Z. Xiao, S. Zhai, Dual-wastes derived biochar with tailored surface features for highly efficient p-nitrophenol adsorption, *J. Clean. Prod.* 353 (2022), 131571, <https://doi.org/10.1016/j.jclepro.2022.131571>.
- [37] P. Lyu, L. Li, X. Huang, G. Wang, C. Zhu, Pre-magnetic bamboo biochar cross-linked CaMgAl layered double-hydroxide composite: high-efficiency removal of As(III) and Cd(II) from aqueous solutions and insight into the mechanism of simultaneous purification, *Sci. Total Environ.* 823 (2022), 153743, <https://doi.org/10.1016/j.scitotenv.2022.153743>.
- [38] M.-S. Kuo, A.J. Mort, A. Dell, Identification and location of 1-glycerate, an unusual acyl substituent in gellan gum, *Carbohydr. Res.* 156 (1986) 173–187, [https://doi.org/10.1016/S0008-6215\(00\)90109-5](https://doi.org/10.1016/S0008-6215(00)90109-5).
- [39] A. Baawad, S. Dhameri, J. Park, K. Murphy, D.-S. Kim, Rheological properties and decomposition rates of gellan gum/hyaluronic acid/β-tricalcium phosphate mixtures, *Int. J. Biol. Macromol.* 211 (2022) 15–25, <https://doi.org/10.1016/j.ijbiomac.2022.05.034>.
- [40] L. Zhengzhou Cinogel Biotech Co, A Good Overview Of Scientific, Technical And Commercial Aspects For Gellan Gum, 2022. Accessed 06/27/2022, <https://www.cinogel.com/p/gellan-gum-overview.html>.
- [41] F. Yamamoto, R.L. Cunha, Acid gelation of gellan: effect of final pH and heat treatment conditions, *Carbohydr. Polym.* 68 (3) (2007) 517–527, <https://doi.org/10.1016/j.carbpol.2006.11.009>.
- [42] R. Balasubramanian, S.S. Kim, J. Lee, Novel synergistic transparent k-Carrageenan/Xanthan gum/Gellan gum hydrogel film: mechanical, thermal and water barrier properties, *Int. J. Biol. Macromol.* 118 (2018) 561–568, <https://doi.org/10.1016/j.ijbiomac.2018.06.110>.
- [43] K. Nishinari, *Physical Chemistry and Industrial Application of Gellan*, Springer Berlin, Heilderberg, Germany, 1999, <https://doi.org/10.1007/3-540-48349-7>.
- [44] K. Arun Krishna, B. Vishalakshi, Gellan gum-based novel composite hydrogel: evaluation as adsorbent for cationic dyes, *J. Appl. Polym. Sci.* 134 (47) (2017) 45527, <https://doi.org/10.1002/app.45527>.
- [45] C. Modrogn, A.M. Pandele, C. Bobirică, D. Dobrotă, A.M. Dăncilă, G. Gârleanu, O.D. Orbuț, C. Borda, D. Gârleanu, C. Orbeci, Synthesis, characterization and sorption capacity examination for a novel hydrogel composite based on gellan gum and graphene oxide (GG/GO), *Polymers* 12 (5) (2020) 1182.
- [46] N. Lázaro, A.L. Sevilla, S. Morales, A.M. Marqués, Heavy metal biosorption by gellan gum gel beads, *Water Res.* 37 (9) (2003) 2118–2126, [https://doi.org/10.1016/S0043-1354\(02\)00575-4](https://doi.org/10.1016/S0043-1354(02)00575-4).
- [47] S. Jana, K.K. Sen, Gellan Gum/PVA Interpenetrating Network Micro-beads for Sustained Drug Delivery, 2nd International Conference on Emerging Materials -

- Characterization and Application (EMCA), in: INDIA, Durgapur, 2019, pp. 614–619.
- [48] A.B. Norton, R.D. Hancock, L.M. Grover, Poly (vinyl alcohol) modification of low acyl gellan hydrogels for applications in tissue regeneration, *Food Hydrocoll.* 42 (2014) 373–377, <https://doi.org/10.1016/j.foodhyd.2014.05.001>.
- [49] S.A. Zaur, B. Vishalakshi, Amphoteric gellan gum-based terpolymer-montmorillonite composite: synthesis, swelling, and dye adsorption studies, *Int. J. Ind. Chem.* 8 (3) (2017) 345–362, <https://doi.org/10.1007/s40090-017-0126-z>.
- [50] K.A. Krishna, B. Vishalakshi, Gellan gum-based novel composite hydrogel: evaluation as adsorbent for cationic dyes, *J. Appl. Polym. Sci.* 134 (47) (2017) 45527, <https://doi.org/10.1002/app.45527>.
- [51] S. Choudhary, K. Sharma, V. Kumar, J.K. Bhatia, S. Sharma, V. Sharma, Microwave-assisted synthesis of gum gellan-cl-poly(acrylic-co-methacrylic acid) hydrogel for cationic dyes removal, *Polym. Bull.* 77 (9) (2020) 4917–4935, <https://doi.org/10.1007/s00289-019-02998-3>.
- [52] M. Zheng, K. Cai, M. Chen, Y. Zhu, L. Zhang, B. Zheng, pH-responsive poly(gellan gum-co-acrylamide-co-acrylic acid) hydrogel: synthesis, and its application for organic dye removal, *Int. J. Biol. Macromol.* 153 (2020) 573–582, <https://doi.org/10.1016/j.ijbiomac.2020.03.024>.
- [53] J.S. Karthika, B. Vishalakshi, Novel stimuli responsive gellan gum-graft-poly (DMAEMA) hydrogel as adsorbent for anionic dye, *Int. J. Biol. Macromol.* 81 (2015) 648–655, <https://doi.org/10.1016/j.ijbiomac.2015.08.064>.
- [54] L.-F. Wang, J.-W. Rhim, Preparation and application of agar/alginate/collagen ternary blend functional food packaging films, *Int. J. Biol. Macromol.* 80 (2015) 460–468, <https://doi.org/10.1016/j.ijbiomac.2015.07.007>.
- [55] Y.S. Ho, G. McKay, Pseudo-second order model for sorption processes, *Process Biochem.* 34 (5) (1999) 451–465, [https://doi.org/10.1016/S0032-9592\(98\)00112-5](https://doi.org/10.1016/S0032-9592(98)00112-5).
- [56] X. Yang, W. Zhu, Y. Song, H. Zhuang, H. Tang, Removal of cationic dye BR46 by biochar prepared from *Chrysanthemum morifolium* ramat straw: a study on adsorption equilibrium, kinetics and isotherm, *J. Mol. Liq.* 340 (2021), 116617, <https://doi.org/10.1016/j.molliq.2021.116617>.
- [57] J. Crank, *The Mathematics of Diffusion*, 2nd. ed., Oxford University Press, Oxford, U.K., 1975.
- [58] C. Tien, *Adsorption Calculations and Modeling*, Butterworth-Heinemann, Newton, MA, 1994.
- [59] K.H. Chu, Revisiting the temkin isotherm: dimensional inconsistency and approximate forms, *Ind. Eng. Chem. Res.* 60 (35) (2021) 13140–13147, <https://doi.org/10.1021/acs.iecr.1c01788>.
- [60] V. Puccia, M.J. Avena, On the use of the dubinin-radushkevich equation to distinguish between physical and chemical adsorption at the solid-water interface, *Colloid Interface Sci. Commun.* 41 (2021), 100376, <https://doi.org/10.1016/j.colcom.2021.100376>.
- [61] O. Falyouna, O. Eljmal, I. Maamoun, A. Tahara, Y. Sugihara, Magnetic zeolite synthesis for efficient removal of cesium in a lab-scale continuous treatment system, *J. Colloid Interface Sci.* 571 (2020) 66–79, <https://doi.org/10.1016/j.jcis.2020.03.028>.
- [62] H.N. Tran, E.C. Lima, R.-S. Juang, J.-C. Bollinger, H.-P. Chao, Thermodynamic parameters of liquid–phase adsorption process calculated from different equilibrium constants related to adsorption isotherms: a comparison study, *J. Environ. Chem. Eng.* 9 (6) (2021), 106674, <https://doi.org/10.1016/j.jece.2021.106674>.
- [63] S. Suman, D.S. Panwar, S. Gautam, Surface morphology properties of biochars obtained from different biomass waste, *Energy Sources, Part A* 39 (10) (2017) 1007–1012, <https://doi.org/10.1080/15567036.2017.1283553>.
- [64] J.N. Hiremath, B. Vishalakshi, Effective removal of divalent metal ions: synthesis and characterization of pH-sensitive guar gum based hydrogels, *Desalin. Water Treat.* 57 (9) (2016) 4018–4027, <https://doi.org/10.1080/19443994.2014.991757>.
- [65] P. Vashisth, K. Nikhil, P. Roy, P.A. Pruthi, R.P. Singh, V. Pruthi, A novel gellan-PVA nanofibrous scaffold for skin tissue regeneration: fabrication and characterization, *Carbohydr. Polym.* 136 (2016) 851–859, <https://doi.org/10.1016/j.carbpol.2015.09.113>.
- [66] R. Tyagi, P. Sharma, A.K. Lakhera, V. Kumar, Thermal, spectroscopic, SEM and rheological datasets of native and quaternized guar gum, *Data Brief* 30 (2020), 105565, <https://doi.org/10.1016/j.dib.2020.105565>.
- [67] A. Subratti, J.L. Vidal, L.J. Lalgee, F.M. Kerton, N.K. Jalsa, Preparation and characterization of biochar derived from the fruit seed of *Cedrela odorata* L and evaluation of its adsorption capacity with methylene blue, *Sustain. Chem. Pharm.* 21 (2021), 100421, <https://doi.org/10.1016/j.scp.2021.100421>.
- [68] O.V. Ovchinnikov, A.V. Evtukhova, T.S. Kondratenko, M.S. Smirnov, V. Y. Khokhlov, O.V. Erina, Manifestation of intermolecular interactions in FTIR spectra of methylene blue molecules, *Vib. Spectrosc.* 86 (2016) 181–189, <https://doi.org/10.1016/j.vibspec.2016.06.016>.
- [69] E. Taheri, A. Fatehizadeh, E.C. Lima, M. Rezakazemi, High surface area acid-treated biochar from pomegranate husk for 2,4-dichlorophenol adsorption from aqueous solution, *Chemosphere* 295 (2022), 133850, <https://doi.org/10.1016/j.chemosphere.2022.133850>.
- [70] J. Kaur, G. Kaur, Optimization of pH conditions and characterization of polyelectrolyte complexes between gellan gum and cationic guar gum, *Polym. Adv. Technol.* 29 (12) (2018) 3035–3048, <https://doi.org/10.1002/pat.4424>.
- [71] P. Vashisth, V. Pruthi, Synthesis and characterization of crosslinked gellan/PVA nanofibers for tissue engineering application, *Mater. Sci. Eng. C* 67 (2016) 304–312, <https://doi.org/10.1016/j.msec.2016.05.049>.
- [72] K.R. Aadil, A. Nathani, C.S. Sharma, N. Lenka, P. Gupta, Investigation of poly (vinyl) alcohol-gellan gum based nanofiber as scaffolds for tissue engineering applications, *J. Drug Deliv. Sci. Technol.* 54 (2019), 101276, <https://doi.org/10.1016/j.jddst.2019.101276>.
- [73] J.J. Salazar-Rabago, R. Leyva-Ramos, J. Rivera-Utrilla, R. Ocampo-Perez, F. J. Cerino-Cordova, Biosorption mechanism of methylene blue from aqueous solution onto white pine (*Pinus durangensis*) sawdust: effect of operating conditions, *Sustain. Environ. Res.* 27 (1) (2017) 32–40, <https://doi.org/10.1016/j.serj.2016.11.009>.
- [74] H.N. Tran, S.-J. You, H.-P. Chao, Insight into adsorption mechanism of cationic dye onto agricultural residues-derived hydrochars: negligible role of  $\pi$ - $\pi$  interaction, *Korean J. Chem. Eng.* 34 (6) (2017) 1708–1720, <https://doi.org/10.1007/s11814-017-0056-7>.
- [75] J. Hoslett, H. Ghazal, N. Mohamad, H. Jouhara, Removal of methylene blue from aqueous solutions by biochar prepared from the pyrolysis of mixed municipal discarded material, *Sci. Total Environ.* 714 (2020), 136832, <https://doi.org/10.1016/j.scitotenv.2020.136832>.
- [76] A.E. Ofomaja, Kinetics and mechanism of methylene blue sorption onto palm kernel fibre, *Process Biochem.* 42 (1) (2007) 16–24, <https://doi.org/10.1016/j.procbio.2006.07.005>.
- [77] M.S. Yilmaz, Graphene oxide/hollow mesoporous silica composite for selective adsorption of methylene blue, *Microporous Mesoporous Mater.* 330 (2022), 111570, <https://doi.org/10.1016/j.micromeso.2021.111570>.
- [78] M.A. Al-Ghouti, R.S. Al-Absi, Mechanistic understanding of the adsorption and thermodynamic aspects of cationic methylene blue dye onto cellulosic olive stones biomass from wastewater, *Sci. Rep.* 10 (1) (2020) 15928, <https://doi.org/10.1038/s41598-020-72996-3>.
- [79] J. Ghazemi, S. Asadpour, Thermodynamics' study of the adsorption process of methylene blue on activated carbon at different ionic strengths, *J. Chem. Thermodyn.* 39 (6) (2007) 967–971, <https://doi.org/10.1016/j.jct.2006.10.018>.
- [80] B. Ji, J. Wang, H. Song, W. Chen, Removal of methylene blue from aqueous solutions using biochar derived from a fallen leaf by slow pyrolysis: behavior and mechanism, *J. Environ. Chem. Eng.* 7 (3) (2019), 103036, <https://doi.org/10.1016/j.jece.2019.103036>.
- [81] E. Alver, A.U. Metin, F. Brouers, Methylene blue adsorption on magnetic alginate/rice husk bio-composite, *Int. J. Biol. Macromol.* 154 (2020) 104–113, <https://doi.org/10.1016/j.ijbiomac.2020.02.330>.
- [82] P. Jia, H. Tan, K. Liu, W. Gao, Removal of methylene blue from aqueous solution by bone char, *Appl. Sci. Basel* 8 (10) (2018) 1903, <https://doi.org/10.3390/app8101903>.
- [83] E.S. Dragan, D.F.A. Loghin, Enhanced sorption of methylene blue from aqueous solutions by semi-IPN composite cryogels with anionically modified potato starch entrapped in PAAm matrix, *Chem. Eng. J.* 234 (2013) 211–222, <https://doi.org/10.1016/j.cej.2013.08.081>.
- [84] K.Z. Elwakeel, A.M. Elgarahy, A.S. Al-Bogami, M.F. Hamza, E. Guibal, 2-mercaptopbenzimidazole-functionalized chitosan for enhanced removal of methylene blue: batch and column studies, *J. Environ. Chem. Eng.* 9 (4) (2021), 105609, <https://doi.org/10.1016/j.jece.2021.105609>.
- [85] L. Chen, Y. Zhu, Y. Cui, R. Dai, Z. Shan, H. Chen, Fabrication of starch-based high-performance adsorptive hydrogels using a novel effective pretreatment and adsorption for cationic methylene blue dye: behavior and mechanism, *Chem. Eng. J.* 405 (2021), 126953, <https://doi.org/10.1016/j.cej.2020.126953>.
- [86] J. Crank, *The Mathematics of Diffusion*, 2nd. ed., Oxford University Press, Oxford, U.K., 1975.
- [87] W.J. Weber, J.C. Morris, Kinetics of adsorption on carbon from solution, *J. Sanit. Eng. Div.* 89 (2) (1963) 31–60.
- [88] A.A. Selifonov, O.G. Shapoval, A.N. Mikerov, V.V. Tuchin, Determination of the diffusion coefficient of methylene blue solutions in dentin of a human tooth using reflectance spectroscopy and their antibacterial activity during laser exposure, *Opt. Spectrosc.* 126 (6) (2019) 758–768, <https://doi.org/10.1134/s0030400x19060213>.
- [89] D.G. Leaist, The effects of aggregation, counterion binding, and added NaCl on diffusion of aqueous methylene-blue, *Can. J. Chem. Rev.* 66 (9) (1988) 2452–2457, <https://doi.org/10.1139/v88-386>.
- [90] K.Z. Elwakeel, A. Shahat, A.S. Al-Bogami, B. Wijesiri, A. Goonetilleke, The synergistic effect of ultrasound power and magnetite incorporation on the sorption/desorption behavior of Cr(VI) and As(V) oxoanions in an aqueous system, *J. Colloid Interface Sci.* 569 (2020) 76–88, <https://doi.org/10.1016/j.jcis.2020.02.067>.
- [91] R. Rajumon, J.C. Anand, A.M. Ealias, D.S. Desai, G. George, M.P. Saravanakumar, Adsorption of textile dyes with ultrasonic assistance using green reduced graphene oxide: an in-depth investigation on sonochemical factors, *J. Environ. Chem. Eng.* 7 (6) (2019), 103479, <https://doi.org/10.1016/j.jece.2019.103479>.
- [92] K.Z. Elwakeel, A. Shahat, Z.A. Khan, W. Alshitari, E. Guibal, Magnetic metal oxide-organic framework material for ultrasonic-assisted sorption of titan yellow and rose bengal from aqueous solutions, *Chem. Eng. J.* 392 (2020), 123635, <https://doi.org/10.1016/j.cej.2019.123635>.
- [93] M. Breitbach, D. Bathen, Influence of ultrasound on adsorption processes, *Ultrason. Sonochem.* 8 (3) (2001) 277–283, [https://doi.org/10.1016/s1350-4177\(01\)00089-x](https://doi.org/10.1016/s1350-4177(01)00089-x).
- [94] N. Tzabar, H.J.M. ter Brake, Adsorption isotherms and sips models of nitrogen, methane, ethane, and propane on commercial activated carbons and polyvinylidene chloride, *Adsorption* 22 (7) (2016) 901–914, <https://doi.org/10.1007/s10450-016-9794-9>.
- [95] T.C. Andrade Siqueira, I.Z. da Silva, A.J. Rubio, R. Bergamasco, F. Gasparotto, E. A. de Souza Paccola, N.U. Yamaguchi, Sugarcane bagasse as an efficient

- biosorbent for methylene blue removal: kinetics, isotherms and thermodynamics, *Int. J. Environ. Res. Public Health* 17 (2) (2020) 526, <https://doi.org/10.3390/ijerph17020526>.
- [96] M.T. Amin, A.A. Alazba, M. Shafiq, Comparative study for adsorption of methylene blue dye on biochar derived from orange peel and banana biomass in aqueous solutions, *Environ. Monit. Assess.* 191 (12) (2019) 735, <https://doi.org/10.1007/s10661-019-7915-0>.
- [97] J. Men, H. Shi, C. Dong, Y. Yang, Y. Han, R. Wang, Y. Zhang, T. Zhao, J. Li, Preparation of poly(sodium 4-styrene sulfonate) grafted magnetic chitosan microspheres for adsorption of cationic dyes, *Int. J. Biol. Macromol.* 181 (2021) 810–823, <https://doi.org/10.1016/j.ijbiomac.2021.04.079>.
- [98] Z. Zhang, L. Xu, Y. Liu, R. Feng, T. Zou, Y. Zhang, Y. Kang, P. Zhou, Efficient removal of methylene blue using the mesoporous activated carbon obtained from mangosteen peel wastes: kinetic, equilibrium, and thermodynamic studies, *Microporous Mesoporous Mater.* 315 (2021), 110904, <https://doi.org/10.1016/j.micromeso.2021.110904>.
- [99] N. Ul Alamin, A.S. Khan, A. Nasrullah, J. Iqbal, Z. Ullah, I.U. Din, N. Muhammad, S.Z. Khan, Activated carbon-alginate beads impregnated with surfactant as sustainable adsorbent for efficient removal of methylene blue, *Int. J. Biol. Macromol.* 176 (2021) 233–243, <https://doi.org/10.1016/j.ijbiomac.2021.02.017>.
- [100] J.-P. Hu, Y. Liu, H.-M. Bi, F.-Y. You, P.-T. Xie, Adsorption of methylene blue from aqueous solution by AB-8 macroreticular resin, in: *3rd International Conference on Chemical and Biological Sciences (ICCBS)*, 2016. Amsterdam, Netherlands.
- [101] O. Kerkez, S.S. Bayazit, H. Uslu, A comparative study for adsorption of methylene blue from aqueous solutions by two kinds of amberlite resin materials, *Desalin. Water Treat.* 45 (1–3) (2012) 206–214, <https://doi.org/10.1080/19443994.2012.692057>.
- [102] F. Wang, Y. Wen, T. Bai, The composite hydrogels of polyvinyl alcohol–gellan gum–Ca<sup>2+</sup> with improved network structure and mechanical property, *Mater. Sci. Eng. C* 69 (2016) 268–275, <https://doi.org/10.1016/j.msec.2016.06.084>.
- [103] A.F. Lubambo, L. Ono, V. Drago, N. Mattoso, J. Varalda, M.R. Sierakowski, C. N. Sakakibara, R.A. Freitas, C.K. Saul, Tuning Fe<sub>3</sub>O<sub>4</sub> nanoparticle dispersion through pH in PVA/guar gum/electrospun membranes, *Carbohydr. Polym.* 134 (2015) 775–783, <https://doi.org/10.1016/j.carbpol.2015.08.013>.
- [104] H.Y. Mostafa, A.M.A. El Naggar, E.A. Elshamy, A.S. Farag, A.I. Hashem, Microwave-assisted extraction for refining of petroleum wax distillate feedstock, *J. Clean. Prod.* 228 (2019) 1034–1047, <https://doi.org/10.1016/j.jclepro.2019.04.263>.